

Satellite Data Assimilation of Upper-Level Sounding Channels in HWRf with Two Different Model Tops

ZOU Xiaolei^{1*} (邹晓蕾), WENG Fuzhong² (翁富忠), Vijay TALLAPRAGADA³, LIN Lin⁴ (林琳),
ZHANG Banglin³ (张邦林), WU Chenfeng⁵ (吴陈锋), and QIN Zhengkun⁶ (秦正坤)

¹ *Earth System Science Interdisciplinary Center, University of Maryland, MD 20740, USA*

² *NOAA Center for Satellite Applications and Research, College Park, MD 20740, USA*

³ *NOAA NCEP Environmental Modeling Center, College Park, MD 20740, USA*

⁴ *I. M. Systems Group, Inc., Rockville, MD 20850, USA*

⁵ *Xiamen Meteorological Bureau, Xiamen 361012, China*

⁶ *Nanjing University of Information Science & Technology, Nanjing 210044, China*

(Received October 19, 2014; in final form January 12, 2015)

ABSTRACT

The Advanced Microwave Sounding Unit-A (AMSU-A) onboard the NOAA satellites NOAA-18 and NOAA-19 and the European Organization for the Exploitation of Meteorological Satellites (EUMETSAT) MetOp-A, the hyperspectral Atmospheric Infrared Sounder (AIRS) onboard Aqua, the High resolution Infrared Sounder (HIRS) onboard NOAA-19 and MetOp-A, and the Advanced Technology Microwave Sounder (ATMS) onboard Suomi National Polar-orbiting Partnership (NPP) satellite provide upper-level sounding channels in tropical cyclone environments. Assimilation of these upper-level sounding channels data in the Hurricane Weather Research and Forecasting (HWRF) system with two different model tops is investigated for the tropical storms Debby and Beryl and hurricanes Sandy and Isaac that occurred in 2012. It is shown that the HWRF system with a higher model top allows more upper-level microwave and infrared sounding channels data to be assimilated into HWRF due to a more accurate upper-level background profile. The track and intensity forecasts produced by the HWRF data assimilation and forecast system with a higher model top are more accurate than those with a lower model top.

Key words: model top, data assimilation, satellite, hurricane

Citation: Zou Xiaolei, Weng Fuzhong, Vijay Tallapragada, et al., 2015: Satellite data assimilation of upper-level sounding channels in HWRF with two different model tops. *J. Meteor. Res.*, **29**(1), 001–027, doi: 10.1007/s13351-015-4108-9.

1. Introduction

Tropical cyclogenesis, tropical cyclone (TC) intensity change and movement are controlled by many environmental factors. The motion of a tropical storm is driven mostly by the large-scale environmental steering, which is defined as a weighted average of the environmental winds between 300 and 850 hPa (Carr and Elsberry, 1990; Velden and Leslie, 1991; Chan, 2005; Wu and Zou, 2008). Tropical cyclogenesis and TC intensification are affected by the vertical wind shear defined by the wind difference between 200 and 850

hPa. Although weak shear may aid genesis by forcing synoptic-scale ascent in baroclinic environments (Bracken and Bosart, 2000; Davis and Bosart, 2006), strong vertical wind shears are detrimental to tropical cyclogenesis (McBride and Zehr, 1981; Zehr, 1992) and impede TC intensification (DeMaria, 1996; Gallina and Velden, 2002). There are a number of hypotheses as to what causes the weakening of TC intensity in the presence of strong vertical wind shear. One hypothesis is that vertical wind shear acts to decrease the efficiency of the hurricane heat engine by ventilating the TC eyewall with low-entropy air at mid

Supported by the NOAA Hurricane Forecast Improvement Program (HFIP) and National Natural Science Foundation of China (91337218).

*Corresponding author: xzou1@umd.edu.

©The Chinese Meteorological Society and Springer-Verlag Berlin Heidelberg 2015

levels by eddy fluxes (Simpson and Riehl, 1958; Cram et al., 2007; Marin et al., 2009). Convective downdraft air originating outside eyewall and having the low-entropy air due to evaporative cooling into the boundary layer is advected inwards into the sub-cloud layer of the eyewall by the radial inflow (Powell, 1990; Riemer et al., 2010; Riemer and Montgomery, 2011). Tang and Emanuel (2012) developed a ventilation index, which is defined as product of the environmental vertical wind shear and the non-dimensional midlevel entropy deficit divided by the potential intensity, for evaluating whether ventilation plays a detectable role in current TC climatology. Steering flow, vertical wind shear, an approaching upper-level trough, upper-level eddy angular momentum flux convergence, stratospheric cooling, and quasi-biennial oscillation in the stratosphere are factors that involve atmospheric conditions in the upper troposphere and the stratosphere.

The interaction of upper-level troughs and/or cut-off lows with TCs is another important factor influencing TC intensification (Molinari and Vollaro, 2010; Leroux et al., 2013). An approaching trough may induce significant vertical wind shear, enhance the outflow poleward of the storm, or introduce the cyclonic potential vorticity (PV) into the TC core through advection. The vertical wind shear is usually detrimental and the PV advection into the TC core is usually beneficial to TC intensity (Leroux et al., 2013), and the asymmetric outflow increases the eddy angular momentum flux convergence calculated at 200 hPa over a 300–600-km radial range around the TC center (Molinari and Vollaro, 2010) and leads to TC intensification for storms whose intensity is well below their maximum potential intensity (Pfeffer and Challa, 1981; Challa and Pfeffer, 1990; DeMaria et al., 1993; Bosart et al., 2000). The intensity of TCs could also be affected by the stratospheric cooling associated with climate change (Ramsay, 2013). With stratospheric cooling, the rising heated air would be able to rise even higher than normal and entering the stratosphere, narrowing the eye of the storm. In turn, the outer rainbands of the TC will retract, decreasing the size of the storm while increasing its strength. A strong correlation between decreasing stratospheric temperatures

and increasing hurricane intensity has been found from 25-yr hurricane data records (Emanuel et al., 2013). Cooling near and above the model tropopause (about 90 hPa) modifies the storm's outflow temperature and could increase the potential intensity (PI) at a rate of 1 m s^{-1} per degree cooling with fixed sea surface temperature (SST) (Emanuel, 1986; Bister and Emanuel, 1997). Chan (1995) noted a relationship between the interannual variations in TC activity and the quasi-biennial oscillation in the stratosphere in the western North Pacific. Modeling of TC track and those opposing effects of TC-trough interaction, stratospheric cooling, and the quasi-biennial oscillation in the stratosphere on the environmental factors affecting TC intensification requires a sufficiently high model top to fully capture these stratospheric features and their interactions with troposphere in hurricane environments.

A large amount of remote sensing data from research and operational satellites becomes available for obtaining an improved description of the initial state of the atmosphere in the upper troposphere and stratosphere. The primary source of data includes those upper-level sounding channels from the Advanced Microwave Sounding Unit-A (AMSU-A) onboard NOAA-18, NOAA-19, MetOp-A, and MetOp-B; the High resolution InfraRed Sounder (HIRS) onboard NOAA-19, MetOp-B, and MetOp-A; the hyperspectral Atmospheric Infrared Sounder (AIRS) onboard EOS Aqua; as well as the Advanced Technology Microwave Sounder (ATMS) and the Cross-Track Infrared Sounder (CrIS) onboard Suomi NPP (National Polar-orbiting Partnership) satellite. These six polar-orbiting satellites (NOAA-18, NOAA-19, MetOp-A, Aqua, MetOp-B, and Suomi NPP) provide microwave and infrared radiance observations to the NCEP operational numerical weather prediction (NWP) system more than 12 times daily. These satellite observations have an excellent global coverage and good spatial resolution varying from about 15 km to around 100 km. However, the satellite radiation is contributed from the stratosphere and the assimilation of the data into NWP requires that the model top be placed at a sufficiently high altitude. For this reason, the ECMWF

model top was raised from 10 hPa to about 0.1 hPa in 1999 (Untch et al., 1999).

It is well known that direct assimilation of satellite infrared (McNally et al., 2006) and microwave (Derber and Wu, 1998) radiances provided by the polar-orbiting meteorological satellites out-performed the assimilation of temperature and moisture retrievals for NWP forecasts. Radiance measurements from different satellites instruments are now routinely assimilated in operational global medium-range forecast modeling systems, which have brought significantly positive impacts on the medium-range forecast (3–7 days). Positive impacts of satellite data assimilation for short-range forecasts using mesoscale regional models have also been demonstrated by several studies. For examples, assimilation of AMSU-A radiance observations and conventional observations using the HIGH Resolution Limited Area Model (HIRLAM) four-dimensional variational data assimilation (4D-Var) consistently out-performed the HIRLAM 3D-Var, particularly for cases with strong mesoscale storm developments (Gustafsson et al., 2012). Using the same HIRLAM 4D-Var, Stengel et al. (2009) demonstrated the benefit of a regional NWP model’s analyses and forecasts gained by the assimilation of three of SEVIRI’s infrared channels (i.e., the two water vapor channels located at 6.2 and 7.3 μm , and the CO₂ channel placed around 13.4 μm). Montmerle et al. (2007) investigated the relative impact of geostationary versus polar-orbiting satellites and their possible complementarity using the Aladin/France operational regional 3D-Var system at Météo-France. Radiance observations from the Spinning Enhanced Visible and Infrared Imager (SEVIRI) on board Meteosat-8; AMSU-A radiances from NOAA-15, NOAA-16, and AQUA; AMSU-B radiances from NOAA-16 and NOAA-17; and HIRS radiances from NOAA-17 and the Advanced Infrared Sounder (AIRS) on board the NOAA and AQUA satellites, were assimilated. Analyses were strongly controlled by SEVIRI data in the middle to high troposphere, resulting in a positive impact on forecast scores and predicted precipitation patterns. Weng and Liu (2003) studied the forward radiative transfer and Jacobian modeling in cloudy

atmospheres, and Weng et al. (2007) employed rain-affected microwave radiance observations for hurricane vortex analysis. Positive impacts of a 3D-Var assimilation of the Advanced Technology Microwave Sounder (ATMS) onboard Suomi NPP satellite on hurricane forecasts have also been demonstrated (Zou et al., 2013). The wealth of more accurate remote sensing data from research and operational satellites, the development of more sophisticated hurricane forecasting models, and the availability of more powerful computers, provide unprecedented opportunities to advance further our knowledge, understanding, and forecast skill of TCs.

This study investigates the impact of the altitude of the model top on satellite radiance assimilation and the track and intensity forecasts of tropical storms using the Hurricane Weather Research and Forecasting (HWRF) system. In the following, a brief description of data, the TC case, and the data assimilation and TC forecast model are provided in Section 2. Satellite observation instruments are introduced in Section 3. Impacts of model top on biases of satellite radiance simulation by a radiative transfer model are described in Section 4. Section 5 depicts the case and the HWRF experiment setup. In Section 6, data assimilation results from the HWRF are discussed. Forecast results are presented in Section 7, in which how the tropical storm forecasts are affected by model tops are elaborated. Section 8 presents a summary of this study.

2. A brief description of the HWRF system

This study employs the HWRF system, which has evolved from a single-domain system (Gopalakrishnan et al., 2011), to a doubly nested version (Bozeman et al., 2011; Pattanayak et al., 2011; Zhang et al., 2011; Yeh et al., 2012), and finally a triply nested version (Zhang et al., 2011). The triply nested 2012 version of the HWRF system is configured with a parent domain at 27-km horizontal resolution, an intermediate two-way moving nesting domain at 9 km, and an innermost two-way moving nesting domain at 3 km. The parent, intermediate, and innermost domains have about 750×750 , 238×150 , and 50×50 model grid points,

respectively (Zhang et al., 2011). Both the intermediate and innermost domains are centered at the initial storm location and configured to follow the projected path of the storm. All the three domains of the HWRF have the same 43 hybrid vertical levels with more than 10 model levels located below 850 hPa and a model top located at about 50 hPa. The ghost domain has the same spatial resolution as the intermediate domain but is slightly larger than the intermediate domain. The data assimilation has a model top located at 50 hPa in the 2012 HWRF version, which is raised to 0.5 hPa in this study. It will be demonstrated that a higher HWRF model top is required for HWRF to better assimilate those upper tropospheric and low stratospheric sounding channels even if their weighting functions peak well below 50 hPa, as well as for HWRF to fully describe the physical and dynamical processes in the upper troposphere and the stratosphere that are important for the development,

movement, and intensity change of tropical cyclones.

Figure 1 shows the parent domain, 3X domain, ghost domain, middle nest, and inner nest for forecasting the track and intensity change of tropical storm Debby. The observed track and the surface pressure field from the background field at 1800 UTC 27 June 2012 within the parent domain are also shown. It is seen that the parent domain is sufficiently large for describing TC environmental flow evolution. Both the intermediate and innermost domains are centered at the initial storm location and move on the projected path of the storm to capture storm's inner core structures. The HWRF atmospheric model employs Ferrier microphysics, NCEP global forecast system (GFS) planetary boundary layer physics, SAS deep convection and shallow convection, and Geophysical Fluid Dynamics Laboratory (GFDL) land surface model and radiation. The atmosphere component is coupled to the Princeton Ocean Model (POM) for all three do-

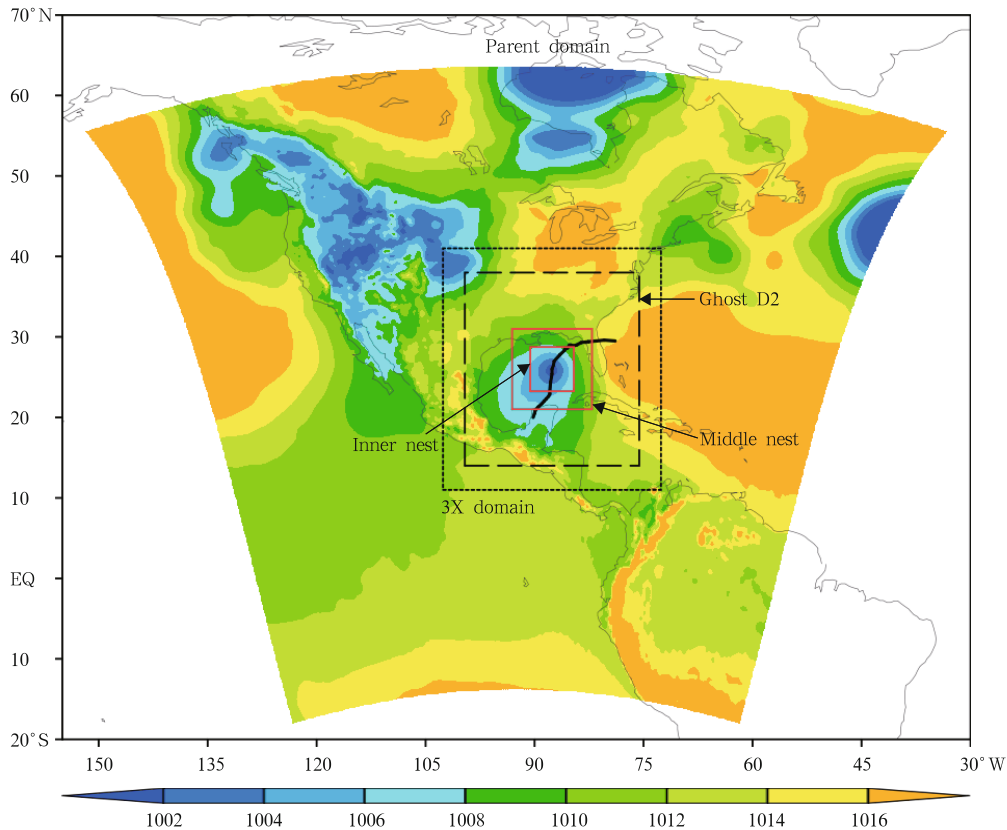


Fig. 1. Sea level pressure (shaded; hPa) from the background field at 1800 UTC 23 June 2012 for tropical storm Debby. The parent domain, 3X domain, ghost domain, middle nest, and inner nest are also indicated. The NHC (National Hurricane Center) best track from 1800 UTC 20 to 1800 UTC 27 June 2012 is indicated in the thick black curve.

mains (Gopalakrishnan et al., 2012).

The NCEP unified Gridpoint Statistical Interpolation (GSI) system employed by the HWRF for data assimilation was described in Derber and Wu (1998) and Wu et al. (2002). A recursive filter was used to obtain a non-homogenous grid-point representation of background errors in the GSI system (Wu et al., 2002; Purser et al., 2003a, b). The Community Radiative Transfer Model (CRTM) developed by the US Joint Center for Satellite Data Assimilation (JCSDA) (Han et al., 2007; Weng, 2007) is used for simulation of all observations from satellite instruments. Satellite data assimilation is carried out in both the parent and the ghost D2 domains at 27- and 9-km resolutions.

The quality control (QC) procedure for each type of satellite data consists of several QC tests to remove outliers under cloudy conditions, outliers associated with uncertainty in surface emissivity, and those field of views (FOVs) with mixed surface types. The GSI bias correction consists of a constant scan bias correction and an air mass bias correction. Spatial data thinning is applied to all ATMS, AMSU-A, HIRS, and AIRS instruments based on the spatial distance between observation and the center of an analysis grid box, the temporal difference between observation and analysis time, terrain height, surface type, etc. A detailed description of the QC, bias correction, and data thinning employed in GSI for ATMS can be found in Zou et al. (2013).

The vortex initialization is performed at the 9-km resolution 3X domain (see Fig. 1). A pre-specified bogus vortex is merged with an environmental field extracted from the GFS analysis. Once the 6-h data assimilation cycle starts, the 6-h HWRF forecasts are used for extracting the environmental fields. The merged field with a corrected vortex and the environment field are the background field for data assimilation that employs the NCEP GSI analysis system.

3. Satellite observations

The AMSU-A onboard both the NOAA and EU-

METSAT polar-orbiting satellites measures the atmospheric radiation in microwave frequency range from 23 to 89 GHz. AMSU-A is a cross-track radiometer. The extreme scan position of the earth view to the beam center is 48.3° . The cross-track size of AMSU-A FOV is 48 km at nadir and that at the outmost scan angle is 105 km. The AMSU-A instruments have 15 channels, in which 3 channels are window channels. Figure 2 presents the normalized weighting functions for AMSU-A channels 1–15, which are overlapped onto the 43 vertical levels of the HWRF model with its model top located at 50 hPa and the 61 vertical levels with its model top located at 0.5 hPa. It is pointed out that the peak of weighting function increases with scan angle. However, such a shift is much smaller for upper-level channels than for low level channels (see Fig. 2 in Zou et al., 2013). The radiative energy measured by AMSU-A primarily comes from the emission of oxygen whose concentration is nearly uniformly distributed through the earth’s atmosphere. Each of the 12 sounding channels provides measurements of a weighted average of radiation emitted from a particular layer of the atmosphere at a specified frequency. The 12 AMSU-A sounding channels are evenly distributed throughout the earth’s atmosphere. Therefore, AMSU-A satellite instruments are ideal for remotely sounding the global atmospheric temperature. More details on the channel characteristics of AMSU-A can be found in Mo (1996) and the NOAA KLM (abbreviated for NOAA-15/16/17) User Guide[Ⓣ].

ATMS is a cross-track microwave radiometer, which scans the earth scene within $\pm 52.7^\circ$ with respect to the nadir direction. It has a total of 22 channels with channels 1–16 designed for atmospheric temperature soundings below about 0.1 hPa and channels 17–22 for atmospheric humidity soundings in the troposphere below approximately 200 hPa (Weng et al., 2012, 2013). The ATMS weighting functions can be found in Weng et al. (2012). Fourteen of ATMS temperature sounding channels (ATMS channels 1–3 and 5–15) have the same frequencies as its predecessor AMSU-A (AMSU-A channels 1–14). The ATMS temperature channel 16 has slightly different frequency

[Ⓣ]<http://www2.ncdc.noaa.gov/docs/klm/c7/sec7-3>

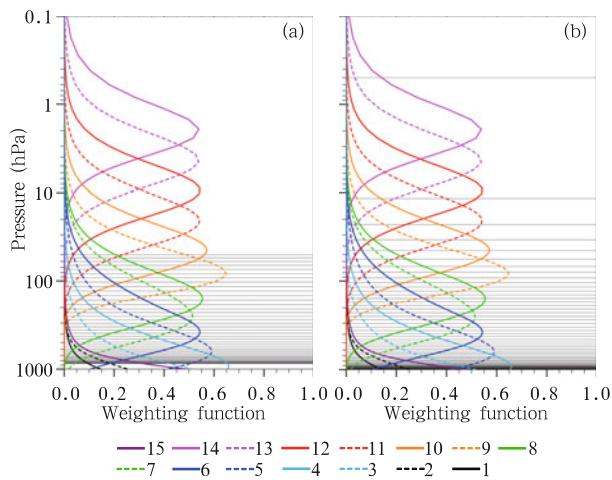


Fig. 2. Weighting functions for AMSU-A channels 1–15 (solid and dashed curves with colors in the legend indicating the channel numbers) overlapped onto the HWRf model levels (gray horizontal line) for (a) the 43-level setup with its model top located at 50 hPa and (b) the 61-level setup with its model top located at 0.5 hPa.

(88.2 GHz) from AMSU-A channel 15 (89.0 GHz). ATMS channel 4 is a new temperature-sounding channel with its central frequency located at 51.76 GHz and contains temperature information in the lower troposphere (around 700 hPa). The ATMS channels 3–16 have a beam width of 2.2° , and the ATMS surface channels 1–2 have a beam width of 5.2° . To reduce the data noise due to a shorter integration time of ATMS FOV, the ATMS overlapping FOVs are re-sampled to AMSU-A-like observations (NWP SAF, 2011; Yang and Zou, 2013).

HIRS is a 20-channel atmospheric sounding instrument with channels 1–12 being located in the longwave infrared frequency range from 6.7 to $15 \mu\text{m}$, channels 13–19 in the shortwave infrared range ($3.7\text{--}4.6 \mu\text{m}$), and channel 20 being a visible channel ($0.6 \mu\text{m}$). HIRS provides a nominal spatial resolution of 20.3 km at nadir in both the visible and shortwave infrared channels and 18.9 km in the longwave infrared channels. The HIRS/4 has the same number of channels as HIRS/3 except for an improvement in observation resolution. The nadir resolution for each HIRS/4 channels is approximately 10 km. Weighting functions for HIRS channels 1–19 overlapped onto the HWRf model levels (gray horizontal line) for the 43-

level setup with its model top located at 50 hPa and the 61-level setup with its model top located at 0.5 hPa are provided in Fig. 3. It is seen that HIRS channels 1–3 are upper-level channels with their peak weighting function located above 100 hPa.

AIRS is a hyperspectral infrared sounder providing a total of 2378 thermal infrared radiance observations across a spectrum from 3.7 to $15.4 \mu\text{m}$. It is one of the six instruments carried onboard the National Aeronautics and Space Administration’s (NASA) Aqua satellite. The spatial resolution for AIRS is 13.5 km at nadir (Aumann et al., 2003). Detailed information on AIRS instrument characteristics was provided by Pagano et al. (2002). A total of 281 AIRS channels are selected for data assimilation in the GSI incorporated in the HWRf. The weighting functions of these 281 channels are provided in Fig. 4. There are more than 65 channels whose weighting functions peak above 100 hPa (Figs. 4a and 4b). There are also several channels whose weighting

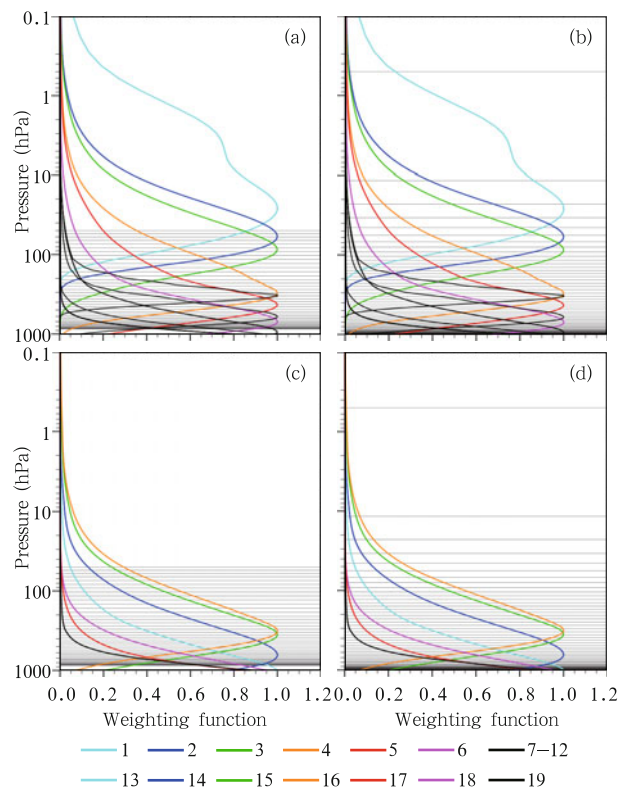


Fig. 3. As in Fig. 2, but for HIRS/4 (a, b) channels 1–12 and (c, d) channels 13–19.

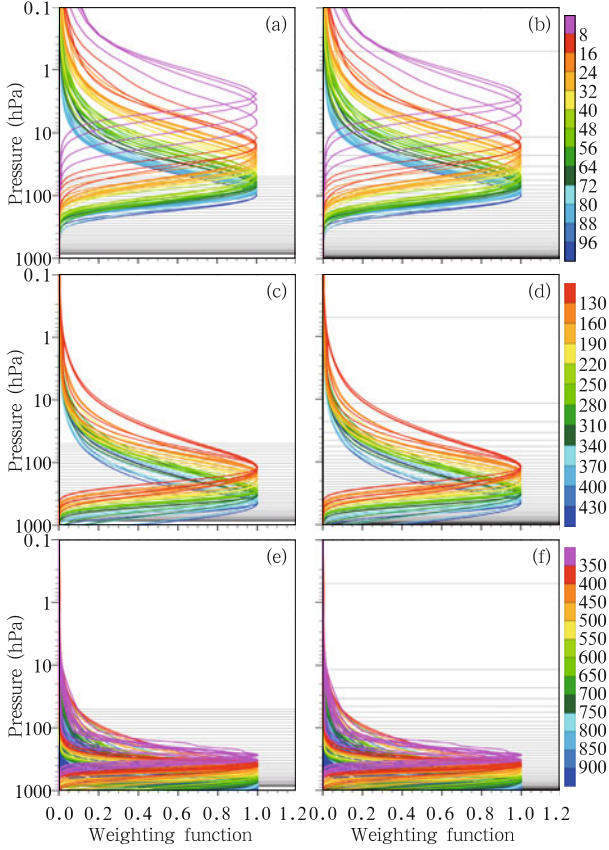


Fig. 4. As in Fig. 2, but for AIRS channels with (a, b) peak weighting function altitude above 100 hPa, (c, d) peak weighting function altitude between 500 and 100 hPa, and (e, f) weighting function values being less than 0.1 at 50 hPa. The peak weighting function altitudes are indicated by the colored legend.

functions peak below 500 hPa but have significant contribution from the atmosphere above 50 hPa (Figs. 4c and 4d). A model top higher than 0.5 hPa with more upper vertical levels is needed to fully resolve upper-level sounding channels of AMSU-A, ATMS, and AIRS.

4. Impacts of model top on biases of satellite radiance simulation by CRTM

The 3D-Var satellite data assimilation searches for a local minimum solution \mathbf{x}^* of the following cost function (Derber and Wu, 1998)

$$\mathbf{J}(\mathbf{x}) = \frac{1}{2}(\mathbf{x} - \mathbf{x}_b)^T \mathbf{B}^{-1}(\mathbf{x} - \mathbf{x}_b) + \frac{1}{2}(\mathbf{H}(\mathbf{x}) - \mathbf{y}^{\text{obs}})^T (\mathbf{O} + \mathbf{F})^{-1}(\mathbf{H}(\mathbf{x}) - \mathbf{y}^{\text{obs}}), \quad (1)$$

where \mathbf{x} is a vector of the control variable, \mathbf{x}_b is a vector of the background state variable, \mathbf{B} is the background error covariance matrix; the vector \mathbf{y} represents all observations including brightness temperature observations from all instruments; the nonlinear vector operator $\mathbf{H}(\mathbf{x})$ represents the forward observation operator that simulates the observed quantities for every given atmospheric state variable \mathbf{x} , \mathbf{O} is the observation error covariance matrix, and \mathbf{F} is the error covariance matrix of the forward observation operator and representativeness error. For satellite radiance data assimilation, the Community Radiative Transfer Model (CRTM) is chosen as $\mathbf{H}(\mathbf{x})$, which calculates the radiance at the top of the atmosphere at different channels from different instruments. The matrices \mathbf{H} and \mathbf{H}^T are the tangent linear operator and the adjoint operator of $\mathbf{H}(\mathbf{x})$, respectively. The state variable \mathbf{x} in Eq. (1) includes the atmospheric temperature profile, water vapor profile, and surface parameters (e.g., sea surface temperature and surface emissivity). A climatology profile is taken as the state variables in CRTM above the model top altitude, which is either 50 or 0.5 hPa in this study. The ozone profiles from the GFS background fields are used as input to CRTM in GSI. A series of surface emissivity/reflectivity models are implemented in CRTM for microwave channels over land (Weng et al., 2001), ocean (Liu et al., 2011), and snow and sea ice (Yan et al., 2004), as well as infrared channels over land (Carter, 2002) and ocean (Wu and Smith, 1997).

Statistically speaking, the analysis obtained by minimizing the cost function defined in Eq. (1) is the maximum likelihood estimate under the assumption that all observations (\mathbf{y}), the background field (\mathbf{x}_b), and the state variable \mathbf{x} are unbiased. Thus, the non-zero mean of observation errors must be subtracted from the data. Since the differences between observations and model simulations, i.e., $\mathbf{O} - \mathbf{B}$, appear together in Eq. (1), only the difference of the observation error mean (μ^o) and the background error mean (μ^b) is required based on the following expression:

$$(\mathbf{O} - \mu^o) - (\mathbf{B} - \mu^b) = \mathbf{O} - \mathbf{B} - (\mu^o - \mu^b). \quad (2)$$

The difference of observation and model biases $\mu^o - \mu^b$

in Eq. (2) can be estimated based on a large sample of $O - B$ statistics since $\overline{O - B} = \overline{O - T} - \overline{(B - T)} = \mu^o - \mu^b$.

If the model top is located too low (e.g., 50 hPa), radiances of many upper-level channels could be difficult to use. Significant temporally and spatially varying biases would be introduced for the assimilation of those channels that have a significant sensitivity to the atmosphere above the model top. If these channels were assimilated and adjusted during the assimilation process, signals in the satellite-observed radiances from above the model top would be aliased, resulting in erroneous adjustments to model initial conditions within the model domain. The quality of forecasts would be reduced. It is thus important to have a relatively higher model top for the TC forecasts to take full advantage of upper-level radiance observations.

A quantitative assessment of the impact of model top altitude on model biases of satellite radiance simulations can be illustrated for ATMS temperature sounding channels. Figure 5a shows a global distribution of the differences of brightness temperature between observations (O) and CRTM simulations (B) for ATMS channel 15 during 0000–1200 UTC 20 December 2011. The 64-level GFS fields were used as input to CRTM. The peak weighting function of ATMS channel 15 is located at 2 hPa. The 64-level GFS model top is around 0.1 hPa. It is seen that the O–B differences are within ± 10 K. However, if the model top is located at 10 hPa, the CRTM will take the US standard profile above 10 hPa as input to produce the simulated ATMS channel 15 brightness temperatures. The resulting differences of brightness temperature between observations and CRTM simulations for ATMS channel 15 are provided in Fig. 5b. The O–B differences could exceed ± 25 K in middle and high latitudes. The upper-level information is crucial to assimilate upper-level channels.

Figure 6 presents the zonal mean temperature differences between GFS 64-level forecast fields and the US standard atmosphere above 10 hPa (Fig. 6a) and the zonal mean brightness temperature differences of ATMS channels 10–15 with and without the GFS fields

above 10 hPa (Fig. 6b). The higher the channel's peak weighting function and the higher the altitude, the larger the O–B brightness temperature biases. The latter is caused by the differences between the GFS fields and the US standard atmosphere. If the model top is located at about 10 hPa, assimilation of ATMS channels 13–15 is in question. This is because the impact of model top altitudes on model simulation of the ATMS upper-level channels is the smallest in the tropics.

5. Case description and the HWRf experiment setup

Tropical storm Debby occurred in 2012 over the Gulf of Mexico, moved into the Atlantic Ocean, and is selected for this investigation. Debby developed from a low-pressure system in the Gulf of Mexico on 23 June

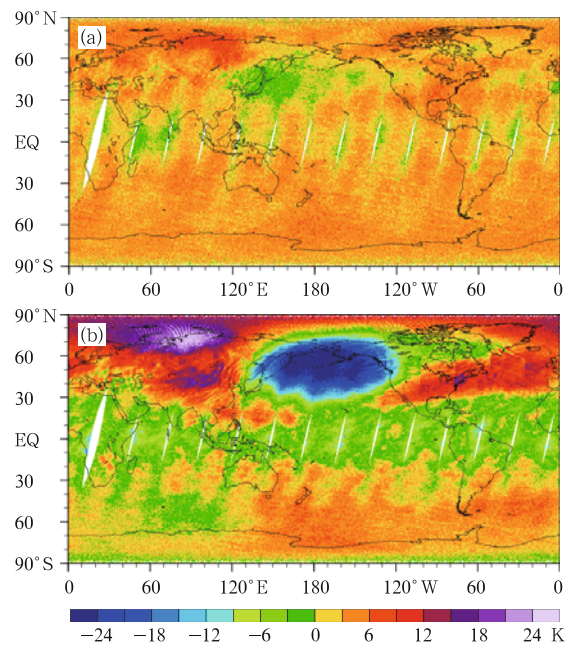


Fig. 5. (a) Global distribution of brightness temperature differences (K) of ATMS channel 15 between observations and model simulation using 64-level GFS fields as input to CRTM during 0000–1200 UTC 20 December 2011. (b) Same as (a) except for using the US standard profile above 10 hPa. Color scheme is identified in the legend. The largest positive values are in violet and the largest negative values (in magnitude) are in blue.

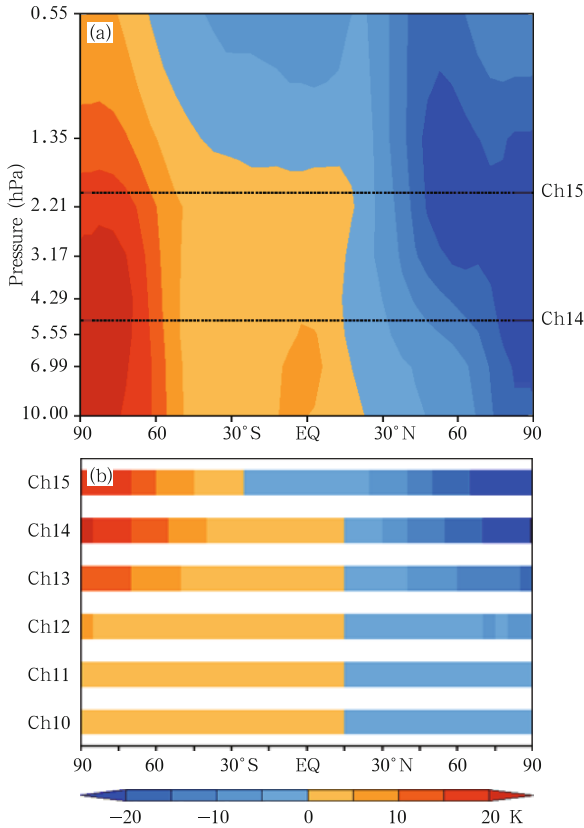


Fig. 6. (a) Zonal mean temperature difference (K) between GFS 64-level forecast fields and the US standard atmosphere above 10 hPa. (b) Zonal mean brightness temperature difference of ATMS channels 10–15 with and without using the GFS fields above 10 hPa.

2012, then moved northeastward over the Gulf of Mexico. It turned into an eastward movement on June 24 when approaching the Gulf coast. Debby made landfall in Florida on June 26. It continued its eastward movement and went across Florida and moved into the Atlantic Ocean. The NCEP operational HWRF 5-day forecast tracks initialized on June 23 and 24 produced a set of westward propagating tracks when Debby moved northeastward. On June 25 and afterward, the operational HWRF model produced reasonably good track forecasts. Therefore, the track prediction of tropical storm Debby before 25 June 2012 was a major challenge.

Although the motion of a tropical storm is affected by many factors, the primary driving force of TC motion is the large-scale environmental steering

(Elsberry, 1995; Wang et al., 1998; Chan, 2005). In order to see under what large-scale flow environment the tropical storm developed and moved, we examine the geopotential and wind vector at 500 hPa using the NCEP global forecast system (GFS) 6-h forecast fields (Fig. 7), which have a horizontal resolution of $0.3125^\circ \times 0.3125^\circ$, a temporal resolution of 6 h, and a total of 64 vertical levels unevenly spaced from the earth's surface to about 0.1 hPa (Kleist et al., 2009). It is seen from Fig. 7 that the tropical storm Debby was located in between a subtropical trough its southeast and a midlatitude ridge its northwest. The anticyclonic flows on the west side of the subtropical high and on the east edge of the midlatitude ridge favored a cyclonic flow development and a low-pressure system in the Gulf of Mexico at 1800 UTC 23 June 2012. The midlatitude ridge experienced an enhanced development with time, preventing Debby's northwestward movement. The subtropical high gradually retreated eastward and the northeast flow in the southwestward branch of the subtropical high and the midlatitude westerly drove Debby to move eastward. It is thus anticipated that an accurate prediction of the size and position of the subtropical high is crucial for the track prediction of Debby when the forecast model is initialized before 25 June 2012.

The model top of the HWRF data assimilation and forecast model is too low for including many upper-level satellite channels in data assimilation. To illustrate this, the 43 vertical levels are indicated in Figs. 2–4 for weighting functions of AMSU-A, HIRS, and AIRS. The weighting function of a channel quantifies the relative contributions to the total measured radiance from different levels of the atmosphere. The measured radiation is most sensitive to the atmospheric temperature at the altitude where weighting function reaches the maximum value. It is seen that a large portion of the weighting functions of many upper-level channels are above the HWRF model top. In order to assimilate more upper-level channels with their weighting functions peaking in the upper troposphere and the stratosphere, the model top is raised to 0.5 hPa, and model levels are increased to 61 accordingly (see right panels of Figs. 2–4).

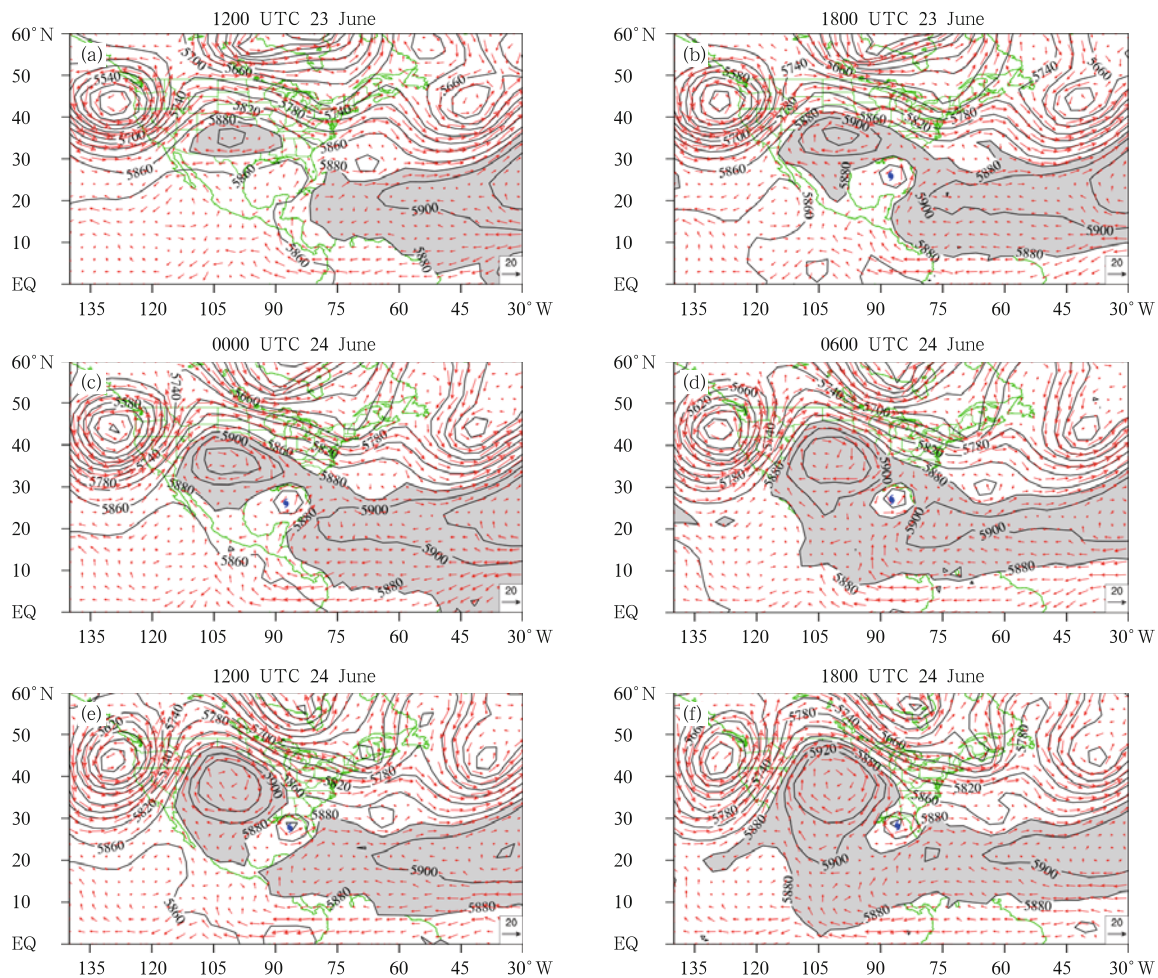


Fig. 7. 500-hPa geopotential height (black curve; m) and wind vector (red vector; m s^{-1}) of the 64-level NCEP GFS data from 1200 UTC 23 to 1800 UTC 24 June 2012. Areas with geopotential height greater than 5880 m are indicated in gray shading.

Two data assimilation and forecast experiments were carried out for tropical storm Debby (2012). The only difference between the two numerical experiments is the model top, which results in different amounts of data assimilated. The model top is located at 50 and 0.5 hPa in experiments L43 and L61, respectively. The model domain information is provided in Fig. 1, in which the sea level pressure from the background field at 1800 UTC 23 June 2012 and the US National Hurricane Center (NHC) best track from 1800 UTC 20 to 1800 UTC 27 June are also shown. In both experiments L43 and L61, AMSU-A, ATMS, HIRS, and AIRS radiance observations, conventional data, the Global Positioning System (GPS) radio occultation (RO) data, and the Advanced Scatterometer AS-

CAT surface wind data are assimilated. The decision of excluding MHS (Microwave Humidity Sounder) and GOES Sounder (GSN) data is made based on a series of data-denying experiments conducted by Qin et al. (2013). Qin et al. (2013) showed that the MHS and GOES imager radiance data assimilation could degrade the forecast skill. Data assimilation experiments are performed on both the parent and intermediate domains at 27- and 9-km resolution, respectively.

6. Data assimilation results

Data assimilation in HWRP/GSI is carried out at 0000, 0600, 1200, and 1800 UTC, which is denoted as t_0 . Observations within $t_0 \pm 1.5$ h are assimilated at

time t_0 , and observations outside these time windows are not assimilated in HWRF/GSI. On the other hand, a polar-orbiting satellite provides global observations twice daily, with the same local equator crossing time (LECT). The polar-orbiting satellites NOAA-18, NOAA-19, Aqua, and Suomi NPP cover the afternoon orbits, and MetOp-A covers the mid-morning orbits. Therefore, satellite data coverage in a fixed HWRF parent model domain (see Fig. 1) from these satellites varies with the UTC time. An example is provided in Fig. 8, which shows the spatial distributions of AMSU-A channel 5 data from NOAA-19 and MetOp-A for experiment L61 with the following 4-time windows: 0000 ± 1.5 , 0600 ± 1.5 , 1200 ± 1.5 , and 1800 ± 1.5 UTC 24 June 2012. Data points from AMSU-A onboard NOAA-19 and MetOp-A that pass

QC and are assimilated in the HWRF/GSI for tropical storm Debby are indicated in orange and cyan, respectively. Data points that do not pass QC are indicated in red dots for both NOAA-19 and MetOp-A. The brightness temperature observations of imager channel 4 from GOES-13 at 2300 UTC 23 June, 0500, 1100, and 1700 UTC 24 June 2012 included in Fig. 8 provide a rough reference for cloud distributions around Debby. It is seen that 1800 UTC has the best data coverage among the 4 UTC times at which data assimilation is carried out. It is also found that cloudy radiances are removed reasonably well. There is a data void area in the central United States from mid-morning and afternoon orbits.

Figure 9 shows data counts of ATMS radiance observations assimilated at 0000, 0600, 1200, and 1800

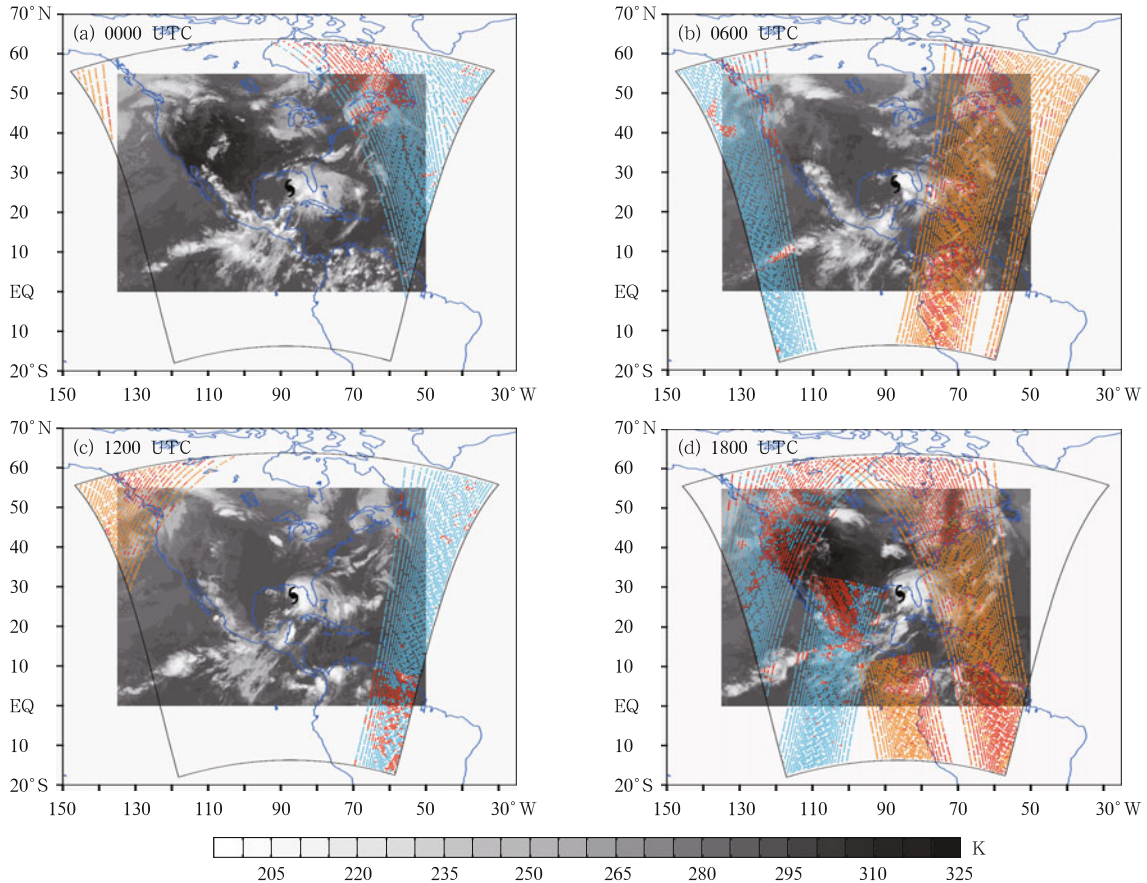


Fig. 8. Spatial distributions of AMSU-A channel 5 data from NOAA-19 (orange dots) and MetOp-A (cyan dots) for experiment L61 at (a) 0000 ± 1.5 UTC, (b) 0600 ± 1.5 UTC, (c) 1200 ± 1.5 UTC, and (d) 1800 ± 1.5 UTC 24 June 2012. Data points that do not pass QC are indicated in red dots for both NOAA-19 and MetOp-A. The HWRF parent domain is indicated by the fan-shaped black curve. Brightness temperature observations of imager channel 4 from GOES-13 at (a) 2300 UTC 23 June, (b) 0500, (c) 1100, and (d) 1700 UTC 24 June 2012 are shown in black shading.

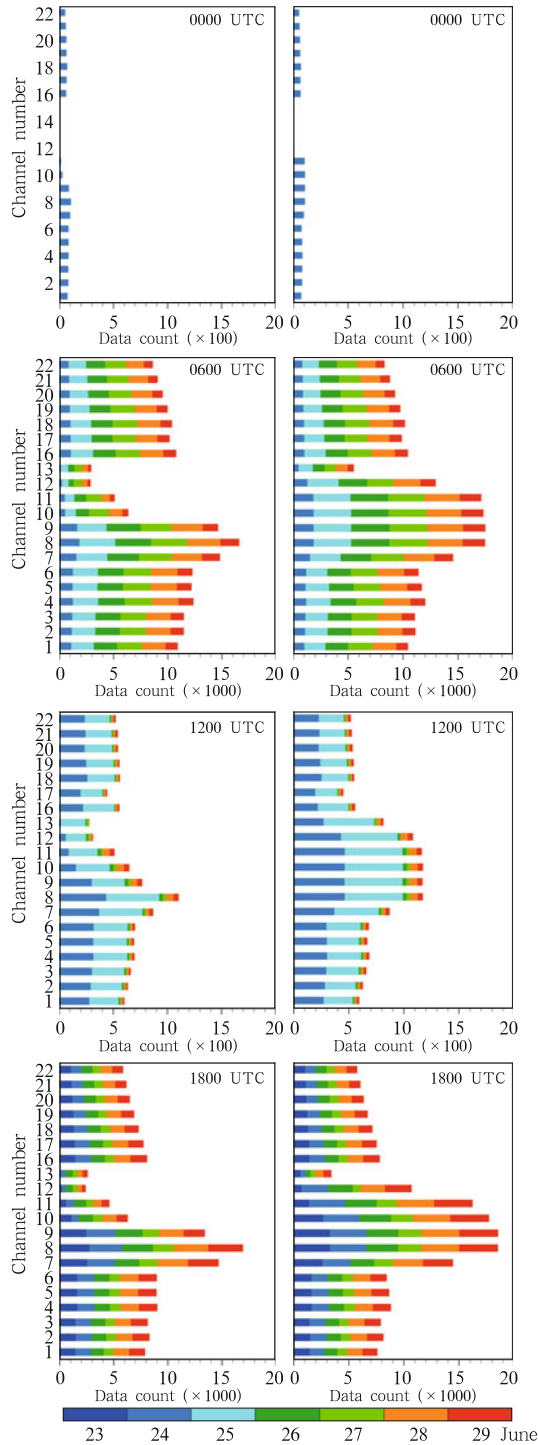


Fig. 9. Channel and time dependence of data counts of ATMS radiance observations assimilated at 0000, 0600, 1200, and 1800 UTC during the entire data assimilation cycle from 23 to 29 June for tropical storm Debby in the parent domain of experiment L43 (left panels) and experiment L61 (right panels).

UTC during the entire data assimilation cycle from 23 to 29 June for tropical storm Debby in the parent domain for both experiments L43 and L61. Very little data are available in the model domain at 0000 UTC from an afternoon orbit Suomi NPP satellite. It is seen that more observations are assimilated for the upper-level channels 8–13 in experiment L61 than those in experiment L43. The total number of satellite data assimilated for different channels varies daily, which is a combined result of the UTC dependence of satellite data and the cloud distribution over the areas with satellite data. Due to the presence of cloud in the troposphere, less amount of the low and middle tropospheric channels (ATMS channels 1–6) are assimilated than the upper-level in experiment L61. The channel dependence of the data counts of AIRS radiance observations assimilated at 3 UTC times (e.g., 0600, 1200, and 1800 UTC) during the data assimilation cycle from 23 to 29 June for tropical storm Debby is presented in Fig. 10 for both experiments L43 and L61. The altitudes of peak weighting function for all AIRS channels assimilated in both experiments are also ind-

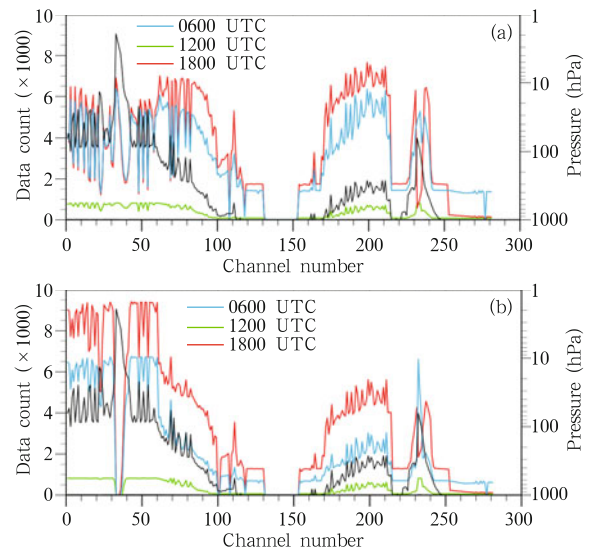


Fig. 10. Channel dependence of data counts of AIRS radiance observations assimilated at different UTC times during the data assimilation cycle from 23 to 29 June for tropical storm Debby in (a) experiment L43 and (b) experiment L61. The peak weighting function is indicated as black line.

icated. It is seen that more upper-level channels and less middle and low tropospheric channels are assimilated in experiment L61 compared with experiment L43. Being consistent with the fact that more afternoon orbit (e.g., AIRS) data are available at 1800 UTC as shown in Fig. 8, the amount of AIRS data assimilated at 1800 UTC is largest within the HWRF domain. Very little and no data are assimilated at 1200 and 0000 UTC, respectively.

Figure 11 presents mean vertical profiles of temperature and specific humidity differences between experiments L43 and L61 at 0600 and 1800 UTC from 23 to 29 June 2012 for tropical storm Debby in the parent domain. With a higher model top, middle and upper tropospheric water vapor tends to be less and upper tropospheric temperature tends to be lower, while low

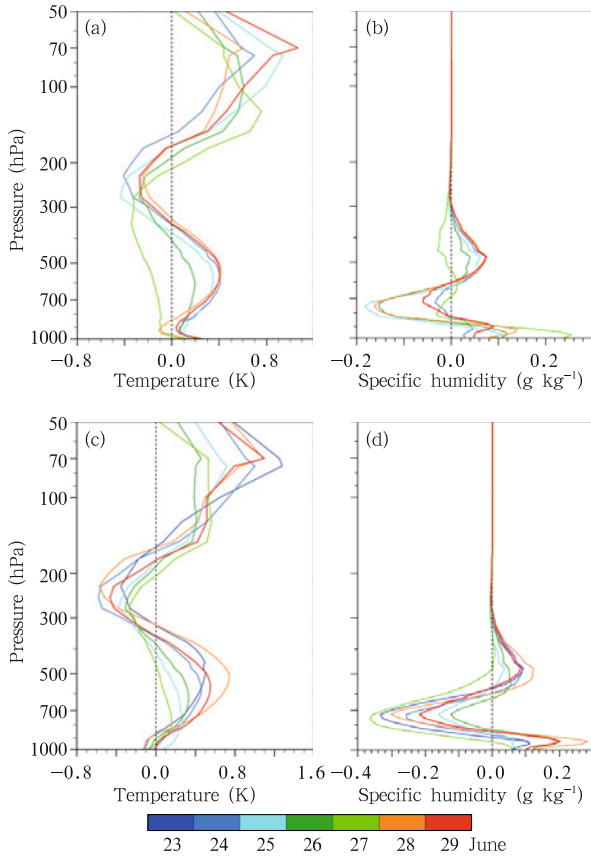


Fig. 11. Mean difference profiles of (a, c) background temperature and (b, d) specific humidity fields between experiments L43 and L61 at (a, b) 0600 UTC and (c, d) 1800 UTC from 23 to 29 June 2012 for tropical storm Debby in the parent domain.

troposphere tends to be wetter and middle and low troposphere tends to be warmer.

The convergence of satellite data assimilation is demonstrated in Figs. 12–16. Figures 12 and 13 provide the differences between observations and the background fields (O–B) and the differences between observations and analysis fields (O–A) of ATMS channels 5–12 at those data points that pass GSI QC and are assimilated at 1800 UTC 24 June 2012 in experiments L61 and L43. Experiment L43 performs similarly to experiment L61 for the middle tropospheric ATMS channels 5–7. Differences of brightness temperatures between ATMS observations and model simulations after data assimilation (O–A; Figs. 12b and 12d) are significantly smaller than the O–B differences (Figs. 12a and 12c) for all ATMS channels 5–12 in experiment L61 (Fig. 12). There is an area of positive O–B difference near the center of tropical storm Debby for ATMS channels 8–9, indicating that the observed warm core structure in the middle and upper troposphere is stronger than that in the model. Although a significant amount of observations are removed for the stratospheric ATMS channels 10–12, the convergence of ATMS data assimilation in experiment L43 (Fig. 13) for the remaining data kept by GSI QC is not so good as those data assimilated in the L61 experiment. The differences O–A are larger than the differences O–B for the stratospheric ATMS channels 10–12 in experiment L43, which is caused by adjusting the temperature below the model top for radiation energy contributions from above the model top. As mentioned before, the US standard atmosphere is used in CRTM for brightness temperature simulations above the model top. The convergence of the low stratospheric and upper tropospheric ATMS channels 8–9 in experiment L43 seems also affected by the model top due to residual radiation energy contributions above the 50-hPa model top to these two channels. Therefore, it is concluded that the poor performance of the L43 compared to the L61 is not solely because of lower model top but also a poor quality control in assimilating the higher-level channels. A revised bias correction may be helpful for assimilation of those upper-level channels to fill the gap between observation and back-

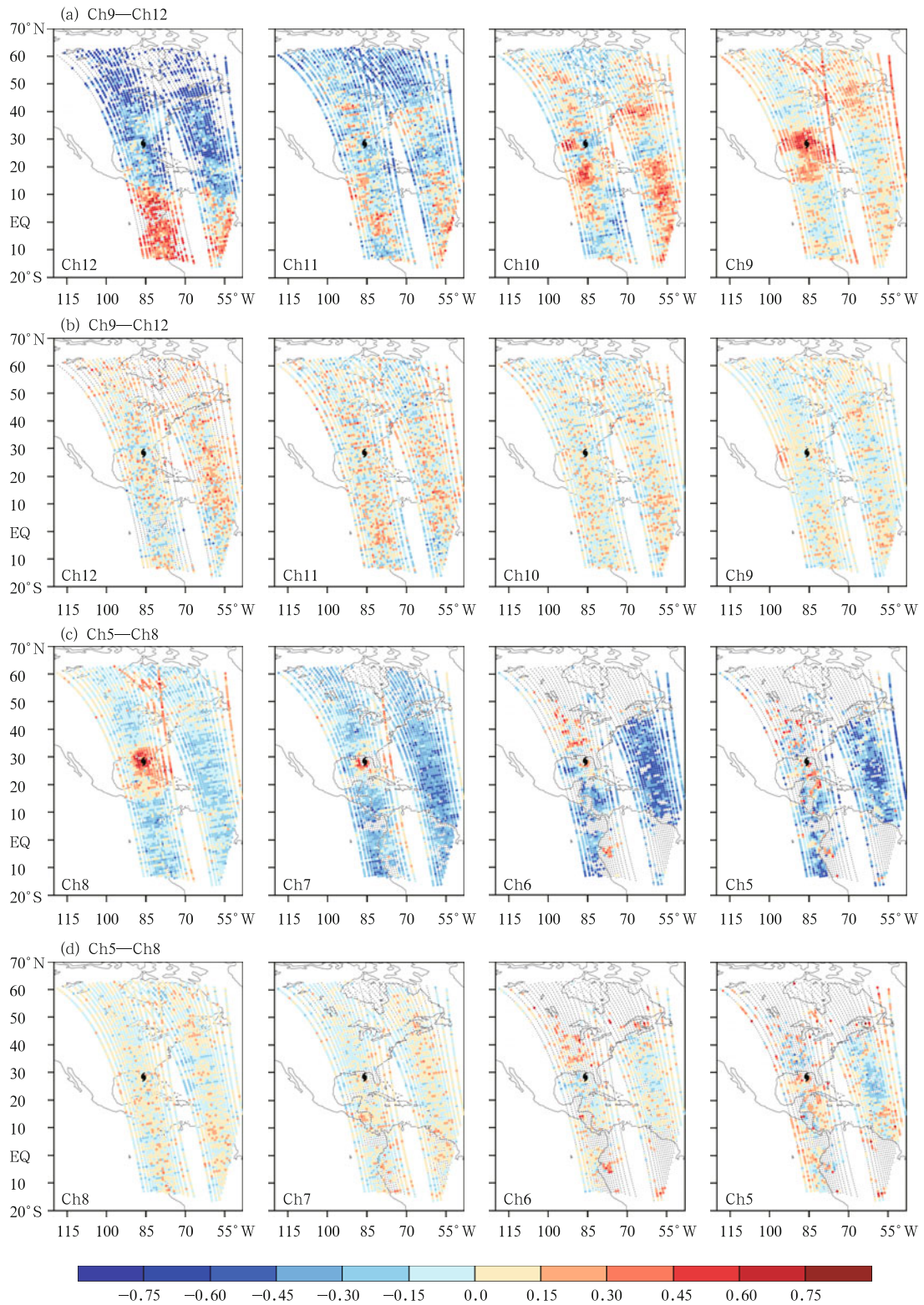


Fig. 12. (a, c) Differences between observations and the background fields (O-B) and (b, d) differences between observations and analysis fields (O-A) of ATMS channels 5–12 at those data points assimilated at 1800 UTC 24 June 2012 in experiment L61. Positive differences are in red and negative values are in blue.

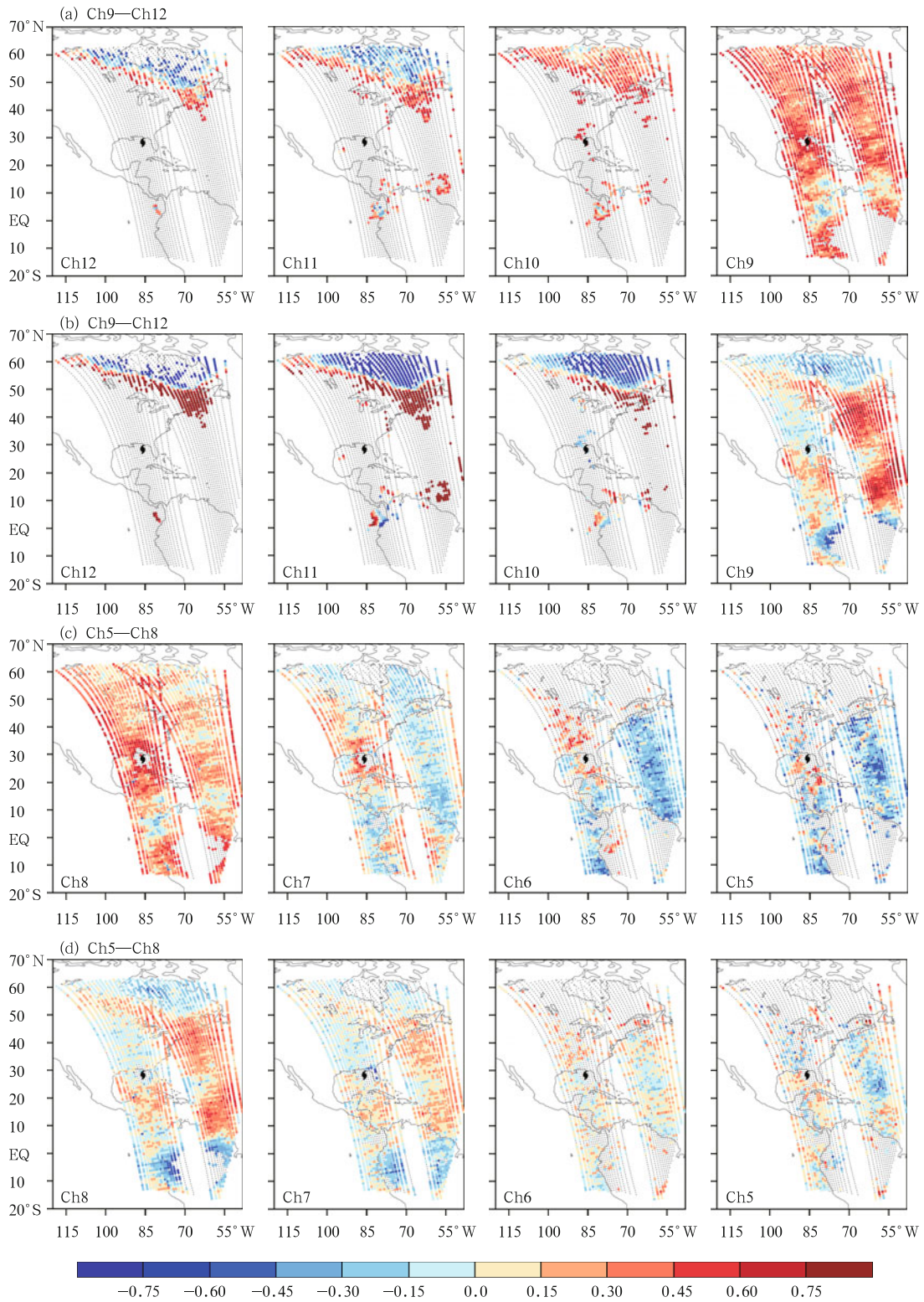


Fig. 13. As in Fig. 12, but for experiment L43.

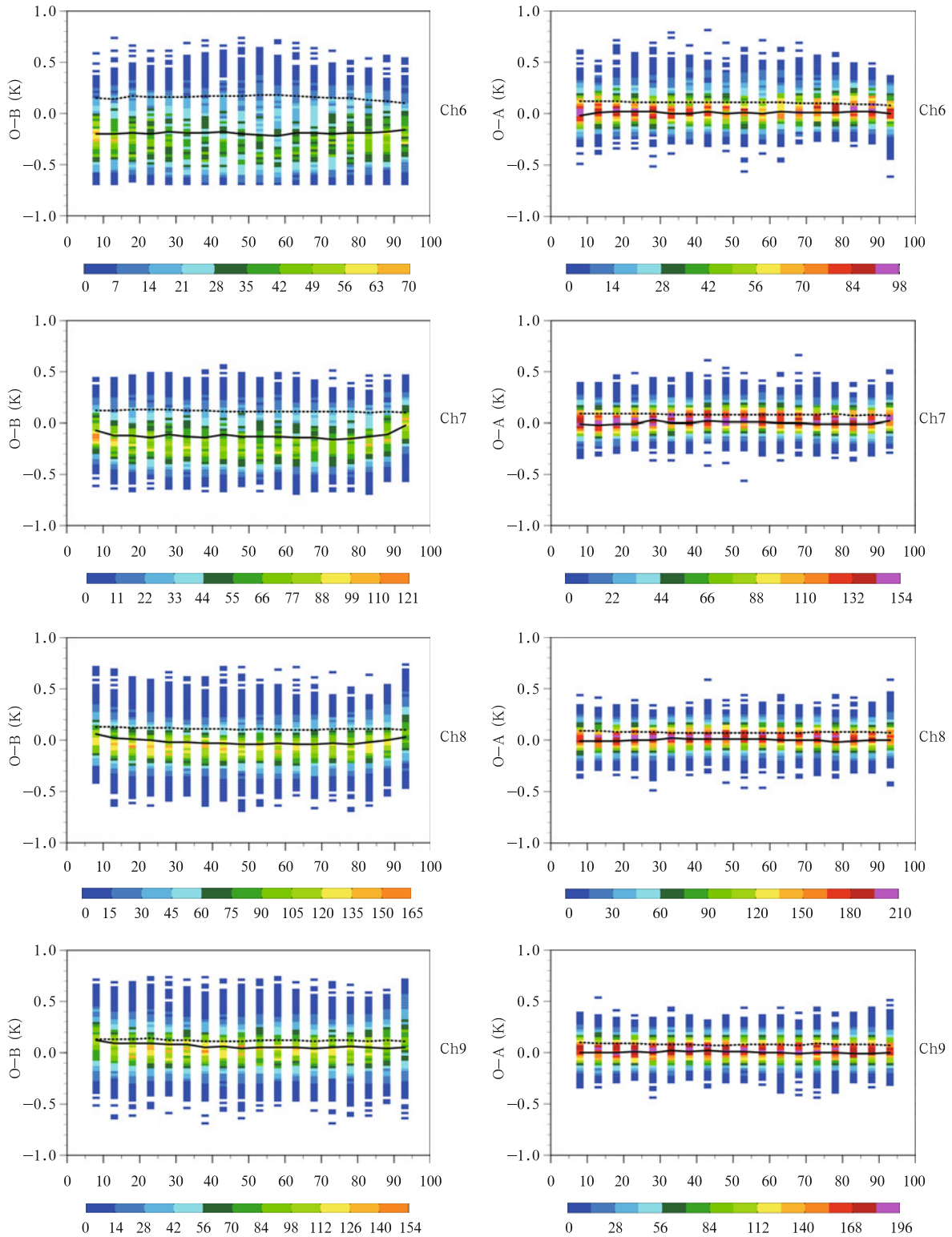


Fig. 14. Data counts calculated at an interval of 0.025 K (color shading) as a function of FOV and the difference between observations and model simulations calculated from the background fields (left panels) and the analysis fields (right panels) for ATMS channels 6–13 in experiment L61 for tropical storm Debby. The angular dependent biases and standard deviations are indicated in solid and dashed curves, respectively.

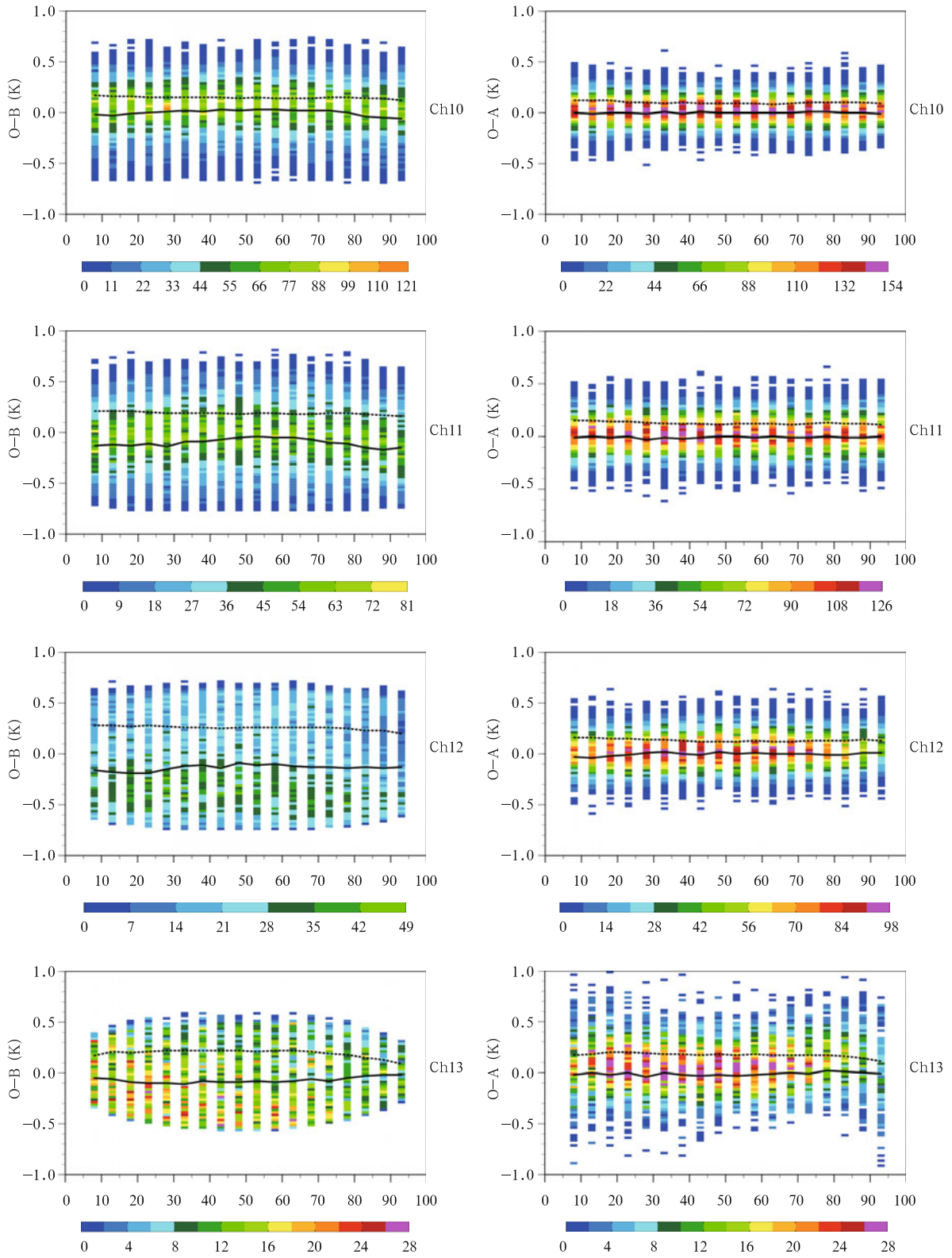


Fig. 14. (Continued)

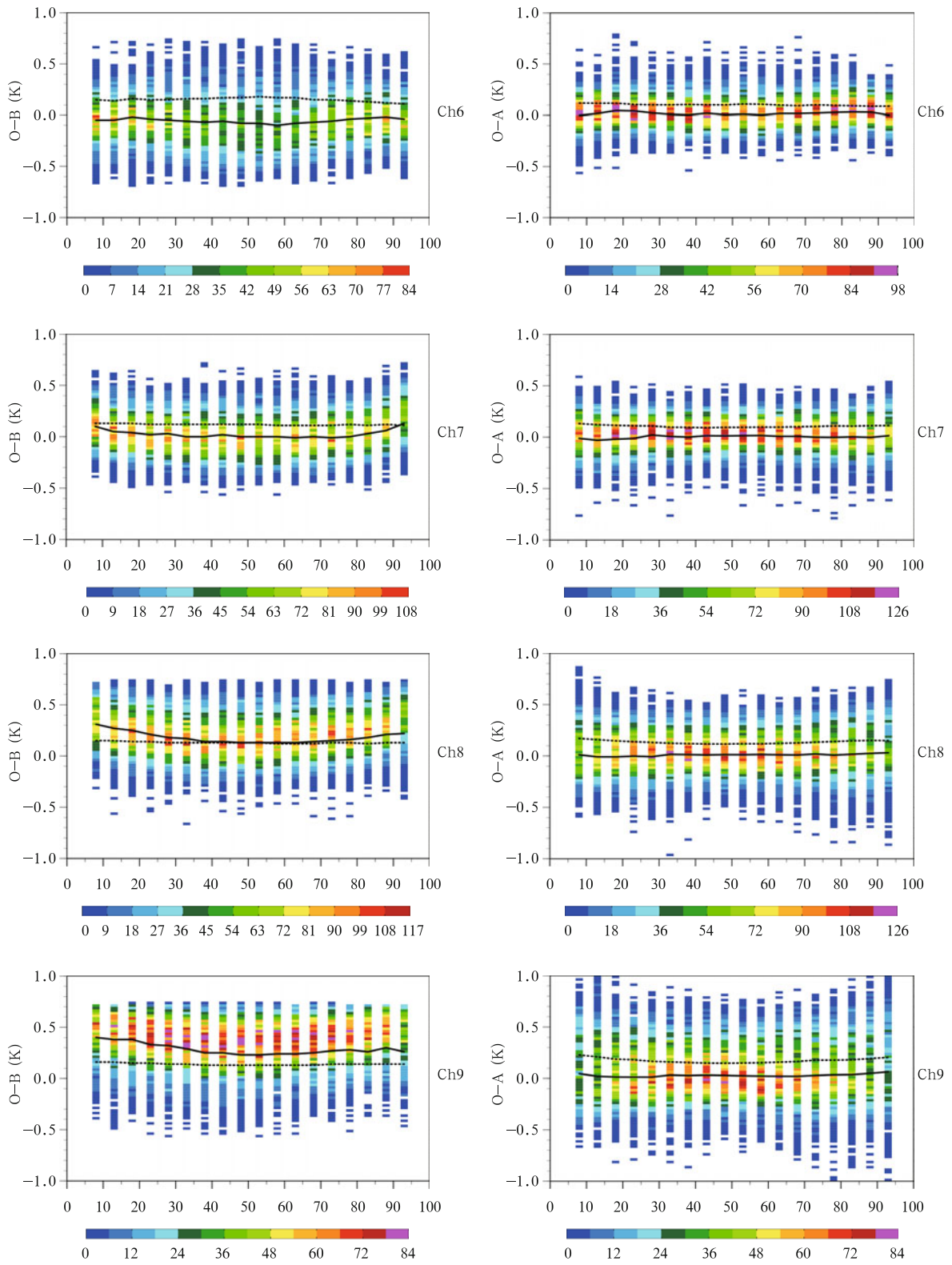


Fig. 15. As in Fig. 14, but for experiment L43.

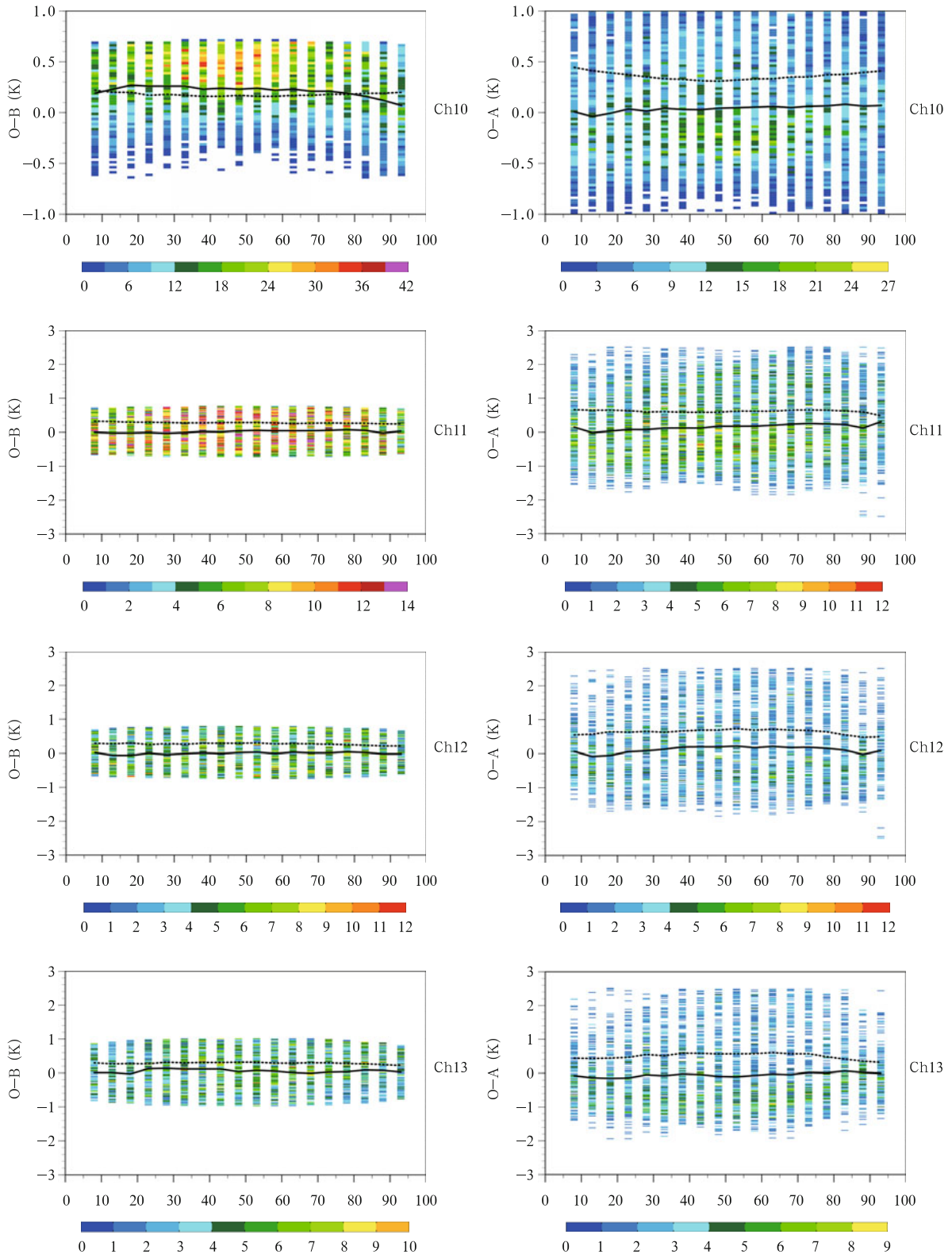


Fig. 15. (Continued)

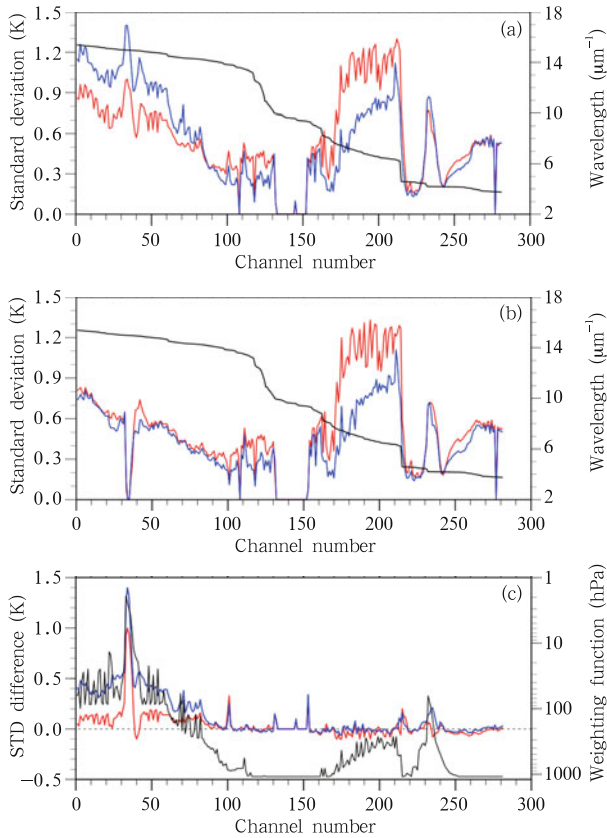


Fig. 16. (a, b) Standard deviations for O–B (red) and O–A (blue) differences of AIRS brightness temperatures in (a) experiment L43 and (b) experiment L61 during the entire data assimilation cycle from 23 to 29 June for tropical storm Debby. (c) The differences of the standard deviations of O–B (red) and O–A (blue) between experiments L43 and L61 (L43 minus L61). The wavelength of each AIRS channel assimilated is indicated in (a, b) in black. The peak weighting function of each AIRS channel assimilated is indicated in (c) in black.

ground. Further investigation on a revised bias correction for assimilation of upper-level channels with a low model top, which could be the case to save computational cost, will be carried out to see if useful information can be provided into model initial conditions instead of simply removing these channels.

Figures 14 and 15 compare the data count distributions as a function of scan angle and the differences O–B or O–A from the 8th to 93th FOV at an interval of 5 FOVs for ATMS channels 6–13 between experiments L43 (Fig. 15) and L61 (Fig. 14). The

angular-dependent biases and standard deviations are also plotted in Figs. 14–15. In experiment L61 (Fig. 14), the O–A data spread is much narrower than that of O–B. The biases and standard deviations are significantly reduced at all scan angles for all ATMS channels 6–13. However, the O–A data spread becomes much broader than that of O–B for ATMS channels 9–13 in experiment L43, which is consistent with Fig. 13. These results confirm an improved fit of NWP model fields to ATMS observations through satellite data assimilation when the model top is raised from 50 to 0.5 hPa, especially for upper-level channels. Similar results are obtained for AIRS data assimilation.

Figure 16 shows a channel-dependent reduction of the differences between AIRS observations and model simulated brightness temperatures after data assimilation, including all data assimilated during 23–29 June for tropical storm Debby in experiments L43 and L61. The wavelength for each of the 281 AIRS channels assimilated in both experiments is also indicated in Fig. 16. Similar to what was seen in microwave upper-level channels, the spread of the differences between observations and model simulations is increased by data assimilation for most AIRS channels whose peak weighting functions are above 100 hPa when the model top is located at 50 hPa (Fig. 16a). The model simulated brightness temperatures based on the analysis compare more favorably to AIRS observations for those channels whose wavelengths are between 6 and 10 μm and peak weighting function altitudes are below 100 hPa. If the model top is raised to 0.5 hPa, the standard deviations of the differences between observations and model simulations are reduced for all channels after satellite data assimilation in experiment L61 (Fig. 16b). Although more AIRS tropospheric channels data are assimilated in L43 than in L61 (see Fig. 10), the convergence (i.e., fit to observations) of L61 is consistently better than that of L43 for almost all AIRS channels assimilated (see Fig. 16c).

7. Forecast differences between the two model tops

The track forecasts by NWP models initialized 2–3 days before the landfall of tropical storm Debby was

a well-known challenge in 2012. The Debby predicted by the operational model moved westward while the real storm moved eastward when the forecasts were initialized before 25 June 2012. Impacts of model top on Debby's track forecasts are shown in Figs. 17 and 18. Figure 17 is a "spaghetti" map showing the observed and model predicted tracks of the 5-day forecasts initialized at 1800 UTC 23 to 1200 UTC 25 June 2012 by the two experiments L43 and L61. The forecast tracks from experiment L43 moved northwestward before 0600 UTC 25 June while the observed track moved northeastward (Fig. 17a). Such a westward track bias is significantly reduced for forecasts in experiment L61 (Fig. 17b) except for the forecast initialized at 1800 UTC 23 and 24 June 2012. It is noticed that the forecast initialized at 1800 UTC 24 June 2012 has produced a track that deviates from the observed track more greatly than the forecasts initialized at earlier times. The main reason is found to be associated

with the fact that the model forecast initialized at 1800 UTC 24 June has a weaker and narrower subtropical high than those from other forecasts.

Figure 18 shows geopotential height and wind vector at 400 and 500 hPa from the analysis at 1800 UTC 24 June and the 6-h forecast initialized at 1200 UTC 24 June 2012 from experiment L61. The areas with the geopotential at 400 hPa being greater than 7590 m and the geopotential at 500 hPa being greater than 5880 m in the 6-h model forecast are significantly broader than those from the analysis at 1800 UTC 24 June 2012. This would alter the environmental steering of modeled tropical storm Debby. A larger geopotential height value at the east side of the tropical storm from the 6-h forecast initialized at 1200 UTC (Figs. 18b and 18d) corresponds to a stronger anticyclonic circulation. The southwestward flows on the west side of the subtropical high would steer the storm to move northeastward.

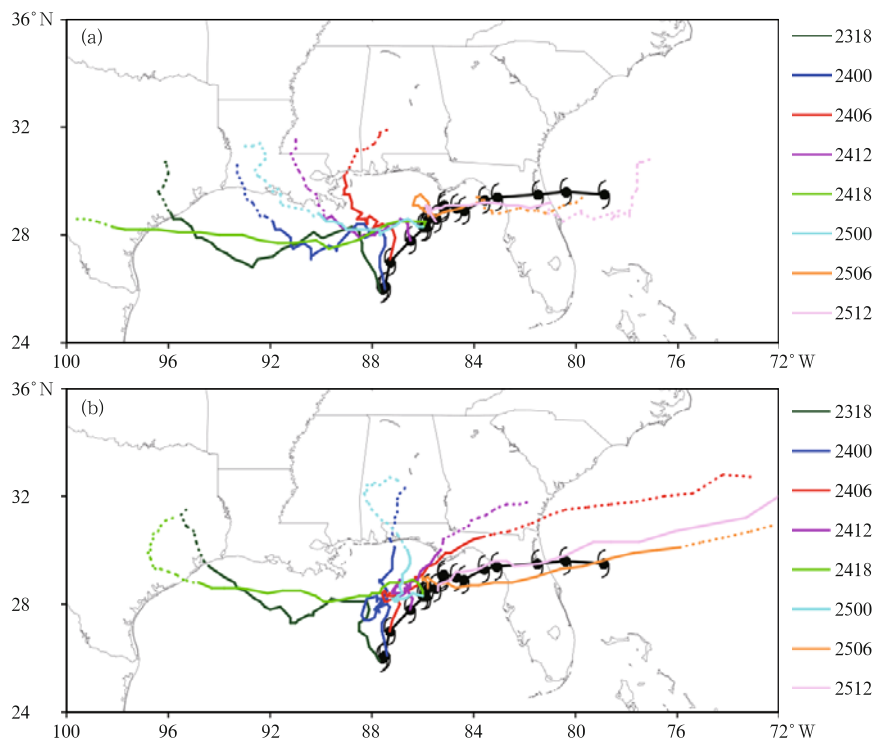


Fig. 17. Five-day forecast tracks (solid and dotted curves with colors in the legend indicating the initial times of model forecasts) of tropical storm Debby from experiments (a) L43 and (b) L61 initialized during 1800 UTC 23–1200 UTC 25 June 2012 at a 6-h interval. The NHC best track is shown in black from 1800 UTC 23 to 1800 UTC 27 June 2012 at a 6-h interval. The model predicted tracks before and after 1800 UTC 27 June 2012 are expressed by solid and dotted curves, respectively.

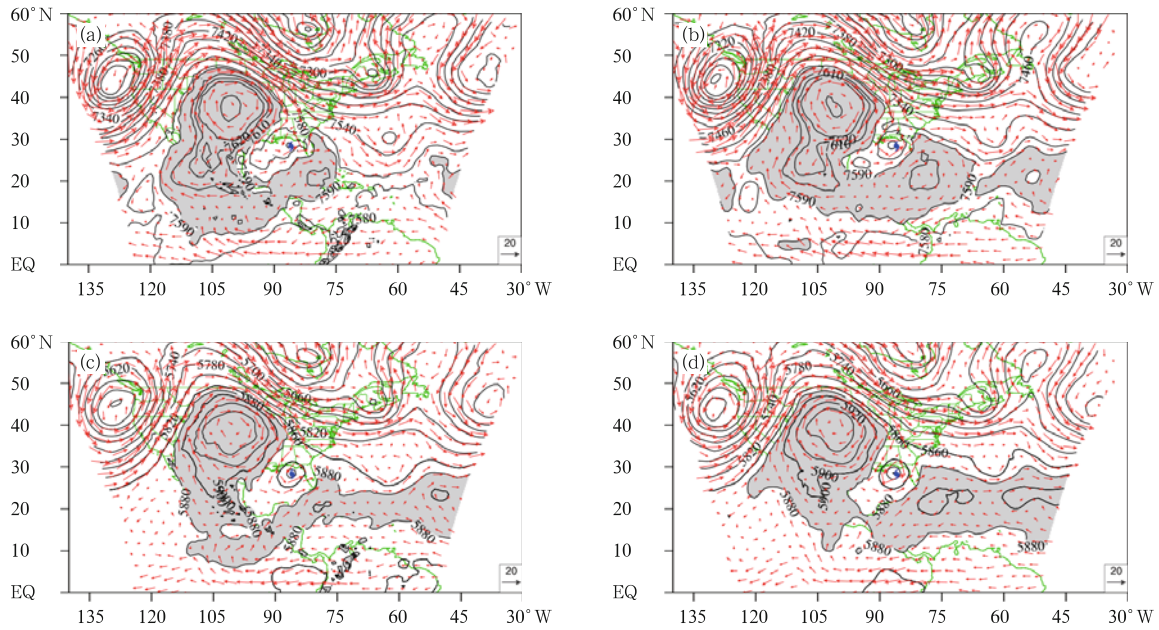


Fig. 18. Geopotential height (black curve; m) and wind vector (red vector; m s^{-1}) at (a, b) 400 and (c, d) 500 hPa from (a, c) the analysis at 1800 UTC 24 June and (b, d) the 6-h forecast initialized at 1200 UTC 24 June 2012 from experiment L61. Areas with geopotential height at 400 and 500 hPa greater than 7590 and 5880 m are shaded.

Although the motion of a tropical storm is affected by many factors, the primary driving force of TC motion is the large-scale environmental steering (Elsberry, 1995; Wang et al., 1998; Chan, 2005). The secondly important factor that controls TC motion is

the effect of the beta drift on TC motion, which not only is much smaller than that of the steering flow, but also produces a systematic northwest track bias from the TC track. The northeastward movement of tropical storm Debby must therefore be controlled

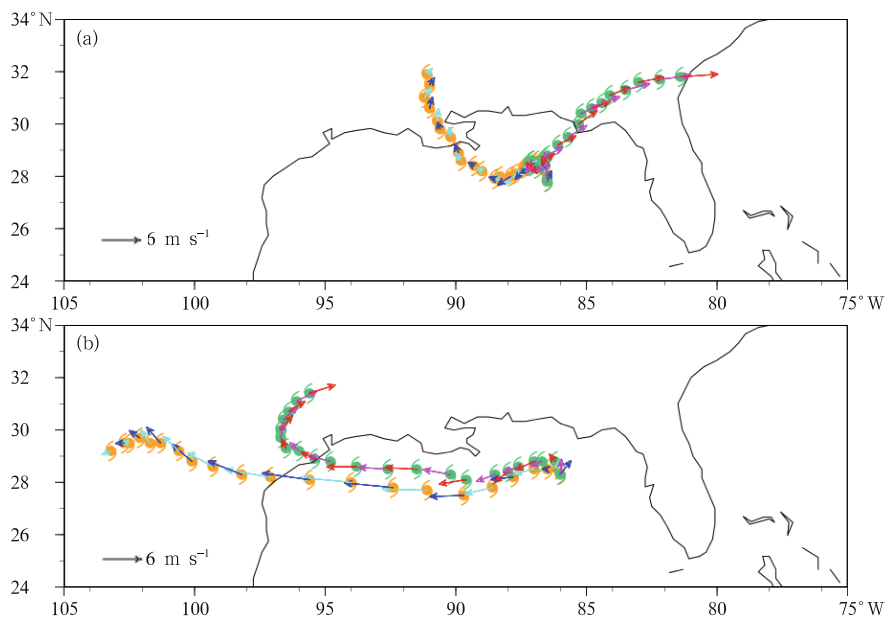


Fig. 19. The forecast tracks and steering flow calculated from the HWRF model forecasts initialized at (a) 1200 and (b) 1800 UTC 24 June 2012 for experiments L43 (blue and cyan arrows over the orange hurricane symbol) and L61 (red and purple arrows over the green hurricane symbol) for tropical storm Debby.

mostly by the environmental flow. Figure 19 provides the 5-day forecast tracks as well as the steering flow calculated from the deep layer mean environmental flow of the HWRf model forecasts initialized at 1200 (Fig. 19a) and 1800 UTC (Fig. 19b) 24 June 2012 for experiments L43 and L61 for tropical storm Debby. For steering flow calculation, the deep layer mean is

first obtained (Carr and Elsberry, 1990; Velden and Leslie, 1991; Wu and Zhou, 2008). The vortex component is then removed by using the Geophysical Fluid Dynamics Laboratory (GFDL) scheme (Kurihara et al., 1993). Finally, the environmental flow within a radius of 500 km from the storm center is averaged to obtain the steering flow. As shown in Fig. 19, the for-

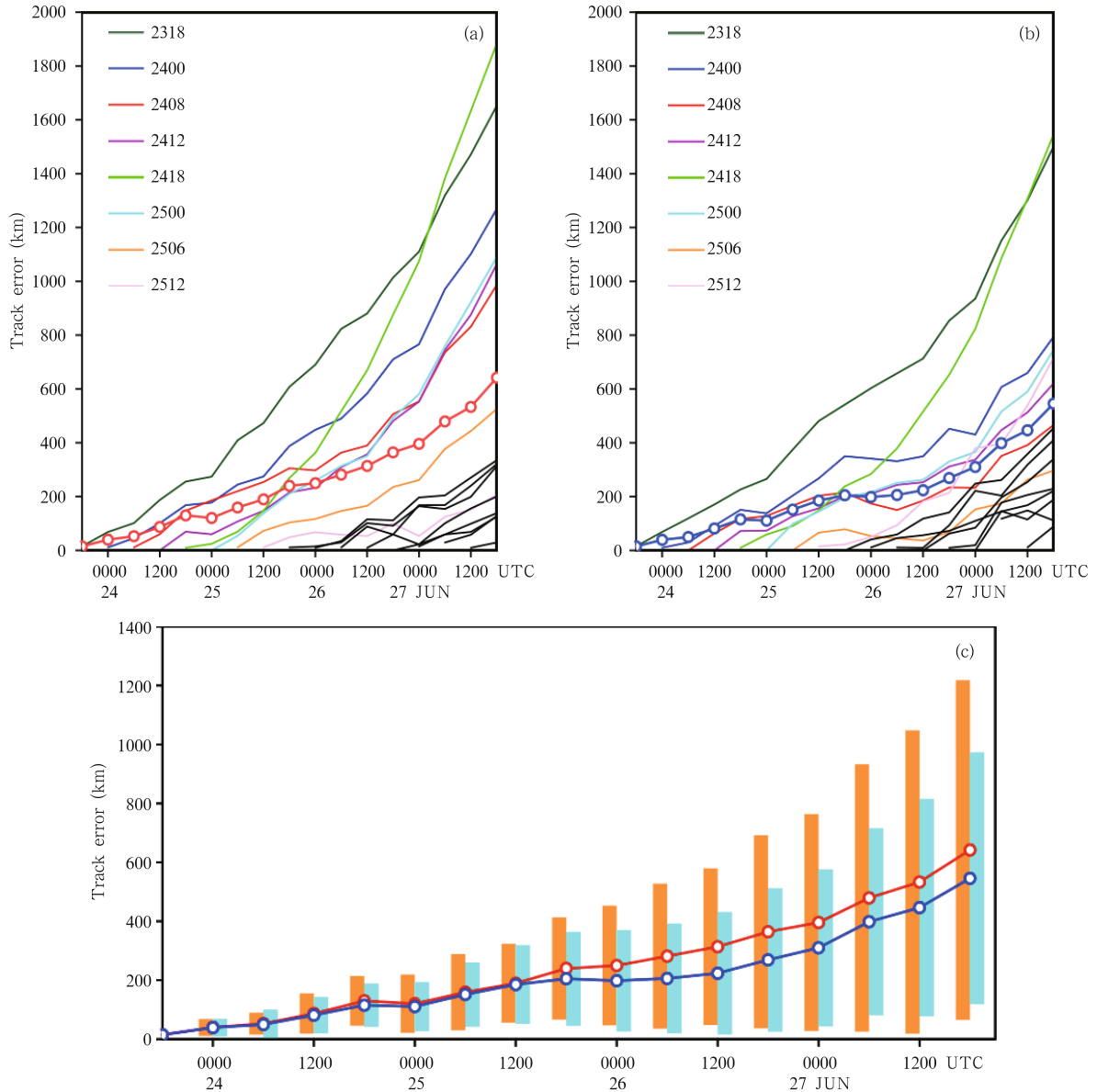


Fig. 20. Spaghetti figures of track errors (km) of all the 5-day forecasts for tropical storm Debby at a 6-h interval from 1800 UTC 23 to 1200 UTC 27 June 2012 as well as the mean error (red and blue curves with circles) by experiments (a) L43 and (b) L61. Colors in the legend indicate the initial times of model forecasts. The track errors for the model forecasts initialized from 1800 UTC 15 to 1200 UTC 27 June 2012 are shown in black curves in (a), (b). (c) The mean (curves) and root-mean-square (bars) errors of the 5-day forecast tracks for tropical storm Debby by experiments L43 (red and orange colors) and L61 (blue and cyan colors).

ecast tracks closely follow the steering flow, confirming that the Debby's motion is mostly driven by the environmental steering flow. In experiment L61, the storm initialized at 1800 UTC moved westward (Fig. 19b) while that from 1200 UTC followed a more realistic northeastward track.

The forecast tracks from experiment L61 at other UTC times followed the observed track more closely. The performance of all the 5-day forecasts for tropical storm Debby initialized from 1800 UTC 23 to 1200 UTC 27 June 2012 is provided in Fig. 20. It is seen that both the mean and the root-mean-square errors of the track forecasts by experiment L61 are smaller than those from experiment L43.

The overall performance of hurricane forecasts with two different model top altitudes for tropical storms Beryl and Debby and hurricanes Isaac and Sandy that made landfall in 2012 is presented in Fig. 21. The time period covered for Beryl, Debby, Isaac, and Sandy is from 0000 UTC 23 to 1200 UTC 30 May, 1800 UTC 23 to 1800 UTC 29 June, 1800 UTC 21 to

1800 UTC 30 August, and 1800 UTC 22 to 1800 UTC 29 October 2012, respectively. Variations of the mean forecast errors and standard deviations with the forecast time are compared between experiments L43 and L61. It is found that the mean errors and standard deviations for both track and intensity forecasts of Beryl, Debby, Isaac, and Sandy are reduced by raising the model top of the HWRF data assimilation system. Further investigation on an optimal setup of different vertical levels for improved satellite data assimilation for hurricane track and intensity forecasts is warranted.

8. Concluding remarks

The present study provides a preliminary assessment of the benefits of having a higher model top in the HWRF/GSI system for both data assimilation and hurricane forecasts. Radiance measurements from AMSU-A, ATMS, AIRS, and HIRS are directly assimilated in the NCEP GSI system, which was adopted by the HWRF system. Specifically, results from satellite radiance assimilation (i.e., ATMS, AMSU-A, AIRS, and HIRS) and conventional data with two different model top altitudes for the forecasts of tropical cyclones in 2012 over the Atlantic Ocean are compared. It is found that satellite radiance data assimilation in the HWRF system with a higher model top improves both the track and intensity forecasts. The improvements brought by a higher model top for data assimilation are more significant when the benchmark HWRF forecasts with a lower model top deviate more from the best track data.

This study only investigates the impacts of direct assimilation of satellite microwave and infrared radiance observations for tropical storm Debby (as well as Beryl and hurricanes Isaac and Sandy but not in much detail). Impacts of satellite radiance assimilation experiments with an appropriately high model top on hurricane track and intensity forecasts could be case dependent and need to be further verified. We plan to repeat these experiments for more Atlantic and Pacific tropical storms in 2012 and 2013 hurricane seasons to see if the conclusions from these limited case studies

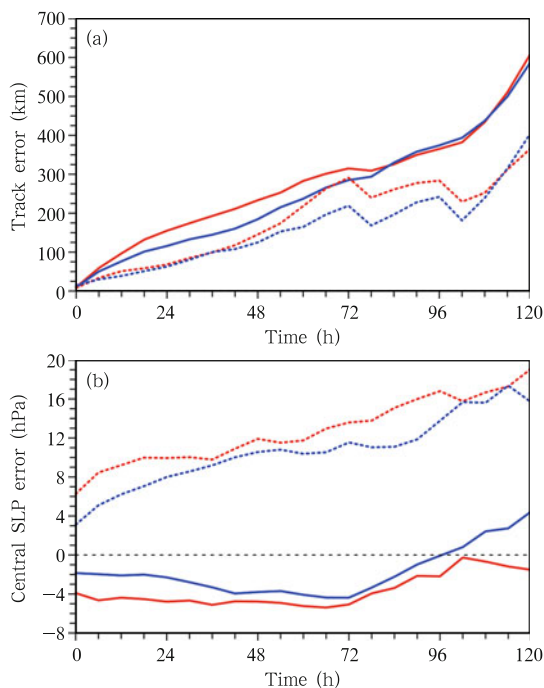


Fig. 21. Mean forecast errors (solid lines) and standard deviations (dotted lines) from experiments L43 (red) and L61 (blue) as functions of forecast lead times for (a) track (km) and (b) central sea level pressure (hPa) of tropical storms Beryl and Debby and hurricanes Isaac and Sandy.

could be generalized.

REFERENCES

- Aumann, H., M. Chahine, and D. Barron, 2003: Sea surface temperature measurements with AIRS: RTG.SST comparison. *SPIE Proc.*, 5151-30, August 2003.
- Bister, M., and K. Emanuel, 1997: The genesis of Hurricane Guillermo: TEXMEX analyses and a modeling study. *Mon. Wea. Rev.*, **125**, 2662–2682.
- Bosart, L. F., C. S. Velden, W. E. Bracken, et al., 2002: Environmental influences on the rapid intensification of Hurricane Opal (1995) over the Gulf of Mexico. *Mon. Wea. Rev.*, **128**, 322–352.
- Bozeman, M. L., D. Niyogi, S. Gopalakrishnan, et al., 2011: An HWRf-based ensemble assessment of the land surface feedback on the post-landfall intensification of Tropical Storm Fay (2008). *Nat. Hazards*, **63**, 1543–1571, doi: 10.1007/s11069-011-9841-5.
- Bracken, W. E., and L. F. Bosart, 2000: The role of synoptic-scale flow during tropical cyclogenesis over the North Atlantic Ocean. *Mon. Wea. Rev.*, **128**, 353–376.
- Carr III, L. E., and R. L. Elsberry, 1990: Observational evidence for predictions of tropical cyclone propagation relative to environmental steering. *J. Atmos. Sci.*, **47**, 542–546.
- Carter, C., Q. Liu, W. Yang, et al., 2002: Net heat flux, visible/infrared imager/radiometer suite algorithm theoretical basis document. Available at http://np_oesslib.ipo.noaa.gov/u_listcategory_v3.php?35.
- Challa, M., and R. L. Pfeffer, 1990: Formation of Atlantic hurricanes from cloud clusters and depressions. *J. Atmos. Sci.*, **47**, 909–927.
- Chan, J. C. L., 1995: Tropical cyclone activity in the western North Pacific in relation to the stratospheric quasi-biennial oscillation. *Mon. Wea. Rev.*, **123**, 2567–2571.
- Chan, J. C. L., 2005: The physics of tropical cyclone motion. *Ann. Rev. Fluid Mech.*, **37**, 99–128.
- Cram, T., J. Persing, M. Montgomery, et al., 2007: A Lagrangian trajectory view on transport and mixing processes between the eye, eyewall, and environment using a high-resolution simulation of Hurricane Bonnie (1998). *J. Atmos. Sci.*, **64**, 1835–1856.
- Davis, C., and L. Bosart, 2006: The formation of Hurricane Humberto (2001): The importance of extra-tropical precursors. *Quart. J. Roy. Meteor. Soc.*, **132**, 2055–2085.
- DeMaria, M., J.-J. Baik, and J. Kaplan, 1993: Upper-level eddy angular momentum flux and tropical cyclone intensity change. *J. Atmos. Sci.*, **50**, 1133–1147.
- DeMaria, M., 1996: The effect of vertical shear on tropical cyclone intensity change. *J. Atmos. Sci.*, **53**, 2076–2087.
- Derber, J. C., and W.-S. Wu, 1998: The use of TOVS cloud-cleared radiances in the NCEP SSI analysis system. *Mon. Wea. Rev.*, **126**, 2287–2299.
- Elsberry, R. L., 1995: Tropical cyclone motion. Global Perspectives of Tropical Cyclones, WMO Report No. TCP-38, Elsberry, R. L., Ed., World Meteorological Organization, Geneva, 106–197.
- Emanuel, K. A., 1986: An air-sea interaction theory for tropical cyclones. Part I: Steady-state maintenance. *J. Atmos. Sci.*, **42**, 1062–1071.
- Emanuel, K. A., S. Solomon, D. Folini, et al., 2013: Influence of tropical tropopause layer cooling on Atlantic hurricane activity. *J. Climate*, **26**, 2288–2301, doi: 10.1175/JCLI-D-12-0024z.1.
- Gallina, G., and C. Velden, 2002: Environmental vertical wind shear and tropical cyclone intensity change utilizing enhanced satellite derived wind information. Preprints, 25th Conf. on Hurricanes and Tropical Meteorology, San Diego, CA, Amer. Meteor. Soc., 172–173.
- Gopalakrishnan, S., F. Marks, X. Zhang, et al., 2011: The experimental HWRf system: A study on the influence of horizontal resolution on the structure and intensity changes in tropical cyclones using an idealized framework. *Mon. Wea. Rev.*, **139**, 1762–1784.
- Gopalakrishnan, S., S. Goldenberg, T. Quirino, et al., 2012: Towards improving high-resolution numerical hurricane forecasting: Influence of model horizontal grid resolution, initialization, and physics. *Wea. Forecasting*, **27**, 647–666.
- Gustafsson, N., X. Y. Huang, X. Yang, et al., 2012: Four-dimensional variational data assimilation for a limited area model. *Tellus*, **64A**, 14985, doi: 0.3402/tellusa.v64i0.14985.
- Han, Y, F. Weng, Q. Liu, et al., 2007: A fast radiative transfer model for SSMIS upper atmosphere sounding channels. *J. Geophys. Res.*, **112**, D11121, doi: 10.1029/2006JD008208.

- Kleist, D. T., D. F. Parrish, J. C. Derber, et al., 2009: Introduction of the GSI into the NCEP Global Data Assimilation System. *Wea. Forecasting*, **24**, 1691–1705.
- Kurihara, Y., M. A. Bender, and R. J. Ross, 1993: An initialization scheme of hurricane models by vortex specification. *Mon. Wea. Rev.*, **121**, 2030–2045.
- Leroux, M.-D., M. Plu, D. Barbary, et al., 2013: Dynamical and physical processes leading to tropical cyclone intensification under upper-level trough forcing. *J. Atmos. Sci.*, **70**, 2547–2565.
- Liu, Q., F. Weng, and S. J. English, 2011: An improved fast microwave water emissivity model. *IEEE Trans. Geosci. Remote Sens.*, **49**, 1238–1250.
- Marin, J., D. Raymond, and G. Raga, 2009: Intensification of tropical cyclones in the GFS model. *Atmos. Chem. Phys.*, **9**, 1407–1417.
- McBride, J., and R. Zehr, 1981: Observational analysis of tropical cyclone formation. Part II: Comparison of non-developing versus developing systems. *J. Atmos. Sci.*, **38**, 1132–1151.
- McNally, A. P., P. D. Watts, J. A. Smith, et al., 2006: The assimilation of AIRS radiance data at ECMWF. *Quart. J. Roy. Meteor. Soc.*, **132**, 935–957.
- Mo, T., 1996: Prelaunch calibration of the Advanced Microwave Sounding Unit-A for NOAA-K. *IEEE Trans. Microwave Theory Technol.*, **44**, 1460–1469, doi: 10.1109/22.536029.
- Molinari, J., and D. Vollaro, 2010: Rapid intensification of a sheared tropical storm. *Mon. Wea. Rev.*, **138**, 3869–3885.
- Montmerle, T., F. Rabier, and C. Fischer, 2007: Relative impact of polar-orbiting and geostationary satellite radiances in the Aladin/France numerical weather prediction system. *Quart. J. R. Meteor. Soc.*, **133**, 655–671.
- NWP SAF, 2011: Annex to AAPP Scientific Documentation: Pre-Processing of ATMS and CrIS, Document NWPSAF-MO-UD-027. Available at <http://research.metoffice.gov.uk/research/interproj/nwpsaf/aapp/index.html>.
- Pagano, T. S., H. H. Aumann, S. E. Broberg, et al., 2002: On-board calibration techniques and test results for the Atmospheric Infrared Sounder (AIRS). Proceedings of SPIE on Earth Observing Systems VII, 7 July 2002, Seattle, USA.
- Pattanayak, S., U. C. Mohanty, and S. G. Gopalakrishnan, 2011: Simulation of very severe cyclone Mala over Bay of Bengal with HWRF modeling system. *Nat. Hazards*, **63**, 1413–1437, doi: 10.1007/s11069-011-9863-z.
- Pfeffer, R. L., and M. Challa, 1981: A numerical study of the role of eddy fluxes of momentum in the development of Atlantic hurricanes. *J. Atmos. Sci.*, **38**, 2393–2398.
- Powell, M., 1990: Boundary layer structure and dynamics in outer hurricane rainbands. Part II: Downdraft modification and mixed layer recovery. *Mon. Wea. Rev.*, **118**, 918–938.
- Purser, R. J., W.-S. Wu, D. F. Parrish, et al., 2003a: Numerical aspects of the application of recursive filters to variational statistical analysis. Part I: Spatially homogeneous and isotropic Gaussian covariances. *Mon. Wea. Rev.*, **131**, 1524–1535.
- Purser, R. J., W.-S. Wu, D. F. Parrish, et al., 2003b: Numerical aspects of the application of recursive filters to variational statistical analysis. Part II: Spatially inhomogeneous and anisotropic general covariances. *Mon. Wea. Rev.*, **131**, 1536–1548.
- Qin, Z., X. Zou, and F. Weng, 2013: Evaluating added benefits of assimilating GOES imager radiance data in GSI for coastal QPFs. *Mon. Wea. Rev.*, **141**, 75–92.
- Ramsay, H. A., 2013: The effects of imposed stratospheric cooling on the maximum intensity of tropical cyclones in axisymmetric radiative-convective equilibrium. *J. Climate*, **26**, 9977–9985, doi: <http://dx.doi.org/10.1175/JCLI-D-13-00195.1>.
- Riemer, M., M. Montgomery, and M. Nicholls, 2010: A new paradigm for intensity modification of tropical cyclones: Thermodynamic impact of vertical wind shear on the inflow layer. *Atmos. Chem. Phys.*, **10**, 3163–3188.
- Riemer, M., and M. Montgomery, 2011: Simple kinematic models for the environmental interaction of tropical cyclones in vertical wind shear. *Atmos. Chem. Phys.*, **11**, 9395–9414.
- Simpson, R., and R. Riehl, 1958: Mid-tropospheric ventilation as a constraint on hurricane development and maintenance. Preprints, Tech. Conf. on Hurricanes, Miami Beach, FL, Amer. Meteor. Soc., D4-1-D4-10.
- Stengel, M., P. Undén, M. Lindskog, et al., 2009: Assimilation of SEVIRI infrared radiances with HIRLAM 4D-Var. *Quart. J. R. Meteor. Soc.*, **135**, 2100–2109.
- Tang, B., and K. Emanuel, 2010: Midlevel ventilation's constraint on tropical cyclone intensity. *J. Atmos. Sci.*, **67**, 1817–1830.

- Untch, A., and A. Simmons, 1999: Increased stratospheric resolution in the ECMWF forecasting system. Proceedings of SODA Workshop on Chemical Data Assimilation. *ECMWF Newsletter*, **82**, 2–8.
- Velden, C. S., and L. M. Leslie, 1991: The basic relationship between tropical cyclone intensity and the depth of the environmental steering layer in the Australian region. *Wea. Forecasting*, **6**, 244–253.
- Wang Bin, R. L. Elsberry, Wang Yuqing, et al., 1998: Dynamics in tropical cyclone motion: A review. *Chinese J. Atmos. Sci.*, **22**, 416–434.
- Weng, F., B. Yan, and N. Grody, 2001: A microwave land emissivity model. *J. Geophys. Res.*, **106**, 20115–20123.
- Weng, F., and Q. Liu, 2003: Satellite data assimilation in numerical weather prediction models. Part I: Forward radiative transfer and Jacobian modeling in cloudy atmospheres. *J. Atmos. Sci.*, **60**, 2633–2646.
- Weng, F., 2007: Advances in radiative transfer modeling in support of satellite data assimilation. *J. Atmos. Sci.*, **64**, 3799–3807.
- Weng, F., T. Zhu, and B. Yan, 2007: Satellite data assimilation in numerical weather prediction models. Part II: Uses of rain-affected radiances from microwave observations for hurricane vortex analysis. *J. Atmos. Sci.*, **64**, 3910–3925.
- Weng, F., X. Zou, X. Wang, et al., 2012: Introduction to Suomi national polar-orbiting partnership advanced technology microwave sounder for numerical weather prediction and tropical cyclone applications. *J. Geophys. Res.*, **117**, D19112, doi: 10.1029/2012JD018144.
- Weng, F., H. Yang, and X. Zou, 2013: On convertibility from antenna to sensor brightness temperature for ATMS. *IEEE Trans. Geo. Remote Sen.*, **10**, 771–775.
- Wu, W.-S., R. J. Purser, and D. F. Parrish, 2002: Three-dimensional variational analysis with spatially inhomogeneous covariances. *Mon. Wea. Rev.*, **130**, 2905–2916.
- Wu, X., and W. L. Smith, 1997: Emissivity of rough sea surface for 8–13 m: Modeling and verification. *Appl. Opt.*, **36**, 2609–2619.
- Wu, Y., and X. Zou, 2008: Numerical test of a simple approach for using TOMS total ozone data in hurricane environment. *Quart. J. R. Meteor. Soc.*, **134**, 1397–1408.
- Yang, H., and X. Zou, 2013: Optimal ATMS remapping algorithm for climate research. *IEEE Trans. Geo. Remote Sensing*, **52**, 7290–7296.
- Yan, B., F. Weng, and K. Okamoto, 2004: Improved estimation of snow emissivity from 5 to 200 GHz. Proceedings of 8th Specialist Meeting on Microwave Radiometry and Remote Sensing Applications, 24–27 February 2004, Rome, Italy.
- Yeh, K.-S., X. Zhang, S. Gopalakrishnan, et al., 2012: The AOML/ESRL hurricane research system: Performance in the 2008 hurricane season. *Nat. Hazards*, **63**, 1439–1449, doi: 10.1007/s11069-011-9787-7.
- Zehr, R., 1992: Tropical Cyclogenesis in the Western North Pacific. NOAA Tech. Rep. NESDIS 61, 181 pp.
- Zhang, X., T. S. Quirino, K.-S. Yeh, et al., 2011: HWRFx: Improving hurricane forecast with high-resolution modeling. *Comput. Sci. Eng.*, **13**, 13–21.
- Zou, X., F. Weng, B. L. Zhang, et al., 2013: Impacts of assimilation of ATMS data in HWRf on track and intensity forecasts of 2012 four landfall hurricanes. *J. Geophys. Res.*, **118**, 11558–11576.
- Zou, X., L. Lin, and F. Weng, 2013: Absolute calibration of ATMS upper level temperature sounding channels using GPS RO observations. *IEEE Trans. Geosci. Remote Sens.*, **52**, 1397–1406.